NUMERICAL MODELING OF FRACTURED SHALE-GAS AND TIGHT-GAS RESERVOIRS USING UNSTRUCTURED GRIDS

A Thesis

by

OLUFEMI MOROUNFOPEFOLUWA OLORODE

Submitted to the Office of Graduate Studies of
Texas A&M University
in partial fulfillment of the requirements for the degree of

MASTER OF SCIENCE

December 2011

Major Subject: Petroleum Engineering

Numerical Modeling of Fractured Shale-Gas and Tight-Gas Reservoirs Using Unstructured Grids

NUMERICAL MODELING OF FRACTURED SHALE-GAS AND TIGHT-GAS RESERVOIRS USING UNSTRUCTURED GRIDS

A Thesis

by

OLUFEMI MOROUNFOPEFOLUWA OLORODE

Submitted to the Office of Graduate Studies of
Texas A&M University
in partial fulfillment of the requirements for the degree of

MASTER OF SCIENCE

Approved by:

Co-Chairs of Committee,	Thomas A. Blasingame
	George J. Moridis
Committee Member,	Vivek Sarin
Head of Department,	Stephen A. Holditch

December 2011

Major Subject: Petroleum Engineering

ABSTRACT

Numerical Modeling of Fractured Shale-Gas and Tight-Gas Reservoirs Using Unstructured Grids.

(December 2011)

Olufemi Morounfopefoluwa Olorode,

B.S., University of Ibadan, Nigeria

Co-Chairs of Advisory Committee, Dr. Thomas A. Blasingame
Dr. George J. Moridis

Various models featuring horizontal wells with multiple induced fractures have been proposed to characterize flow behavior over time in tight gas and shale gas systems. Currently, there is little consensus regarding the effects of non-ideal fracture geometries and coupled primary-secondary fracture interactions on reservoir performance in these unconventional gas reservoirs.

This thesis provides a grid construction tool to generate high-resolution unstructured meshes using Voronoi grids, which provides the flexibility required to accurately represent complex geologic domains and fractures in three dimensions. Using these Voronoi grids, the interaction between propped hydraulic fractures and secondary "stress-release" fractures were evaluated. Additionally, various primary fracture configurations were examined, where the fractures may be non-planar or non-orthogonal.

For this study, a numerical model was developed to assess the potential performance of tight gas and shale gas reservoirs. These simulations utilized up to a half-million grid-blocks and consider a period of up to 3,000 years in some cases. The aim is to provide very high-definition reference numerical solutions that will exhibit virtually all flow regimes we can expect in these unconventional gas reservoirs. The simulation results are analyzed to identify production signatures and flow regimes using diagnostic plots, and these interpretations are confirmed using pressure maps where useful.

The coupled primary-secondary fracture systems with the largest fracture surface areas are shown to give the highest production in the traditional "linear flow" regime (which occurs for very high conductivity vertical fracture cases). The non-ideal hydraulic fracture geometries are shown to yield progressively lower production as the angularity of these fractures increases. Hence, to design optimum fracture completions, we should endeavor to keep the fractures as orthogonal to the horizontal well as possible.

This work expands the current understanding of flow behavior in fractured tight-gas and shale-gas systems and may be used to optimize fracture and completion design, to validate analytical models and to facilitate more accurate reserves estimation.

DEDICATION

This thesis is dedicated to my family and friends.

ACKNOWLEDGEMENTS

I would like to thank Dr. Tom Blasingame for his guidance and high standard of perfection, Dr. George Moridis for sharing his expertise in the course of this research, and Dr. Vivek Sarin for serving as a member of my advisory committee.

This work was supported by RPSEA (Contract No. 07122-23) through the Ultra-Deepwater and Unconventional Natural Gas and Other Petroleum Resources Research and Development Program as authorized by the US Energy Policy Act (EPAct) of 2005.

TABLE OF CONTENTS

LIST OF FIGURES

FIGURE Page

FIGURE Page

FIGURE Page

LIST OF TABLES

CHAPTER I
INTRODUCTION

1.1 Statement of the Problem

The ever-increasing energy demand has prompted a growth in the development of unconventional gas resources. The U.S. Energy Information Administration (U.S. EIA., 2007) stated that natural gas from shale-gas reservoirs accounted for about 6 percent of the gas produced in the U.S. in 2005, and they projected that by 2030, half of the natural gas produced in the U.S. will be from unconventional sources. All these, coupled with the steady rise in natural gas prices has led to increased interest in tight-gas and shale-gas reservoirs (Warlick, 2006).

Several analytical models have been proposed to predict flow performance, while numerical studies have been conducted to evaluate the impact of different reservoir and fracture properties on production. Most of these studies have assumed ideal planar, orthogonal and regular fracture geometries; hence, only very little is little is known about the effects of non-ideal fracture geometries on flow behavior and well performance in these unconventional gas reservoirs.

1.2 Objectives

The objectives of the proposed research are:

- To develop TAMMESH, an unstructured mesh-maker that uses the voro++ library for Voronoi tessellation and calculation of grid-block volumes, centers, connection areas, and other parameters, which are required as input into a numerical simulator.
- To analyze the simulation results of different combinations of fracture permeability and aperture that yield the same fracture conductivity, in an effort to determine whether we can distinguish between fracture permeability and fracture aperture.
- To investigate the implications of a "single-fracture" and "stencil" representation of a multiply-fractured horizontal well.
- To compare the simulation results of planar and "non-planar" hydraulic fractures with the same "apparent" fracture half-length and Stimulated Reservoir Volume (SRV).
- To study the effect of non-orthogonal fracture orientations on the production performance.
- To simulate secondary fractures with planar and non-planar geometries that are orthogonal to the primary network, in order to identify the mechanisms and quantify the impact of the interaction between the primary and secondary fracture networks.

This thesis follows the style of *SPE Reservoir Evaluation & Engineering*.

1.3 Importance

The use of unstructured grids throughout this work provides the capability to capture non-ideal fracture geometries, such as non-orthogonal and non-planar fracture orientations, as well as the interaction between hydraulic and induced fractures. Additionally, the use of these Voronoi grids can help to reduce the computational requirement and duration of a numerical study, and also facilitate the analysis of the results because far fewer cells could be required when compared with regular, refined Cartesian grids.

The study of irregular fracture patterns can provide useful insight into the effects of these non-ideal fracture geometries on the flow behavior, while the evaluation of the single-fracture representation of multiply-fractured horizontal wells can determine whether this approach in analytical or simplified numerical models is appropriate.

A study of the interaction between secondary and primary fractures is also presented to illustrate the impact of these coupled primary-secondary fracture systems on production, and to investigate whether these fracture systems can be represented by an equivalent primary fracture system.

1.4 Reference Reservoir and Completion Parameters

Table 1.1 shows the reservoir and completion parameters used in this work. These parameters are representative of the Barnett shale, and were extracted from publications by Shelley et al., (2010), Houze et al., (2010), and Miller et al. (2010).

Table 1.1—Representative Barnett shale-gas parameters

Parameters	SI Unit	Field Unit
Fracture half-length, x_f	90 m	300 ft
Fracture width, w_f	3 mm	0.00984 ft
Fracture spacing, d_f	100 m	328 ft
Well length, L_w	1200 m	4000 ft
Number of fractures	12	12
Reservoir thickness, h	100 m	330 ft
Permeability, k_{shale}	1.0×10^{-19} m^2	1.0×10^{-4} ft
Fracture permeability, k_{frac}	5.0×10^{-11} m^2	5.0×10^{4} ft
Matrix porosity, ϕ	4 percent	4 percent
Fracture porosity, ϕ_{frac}	33 percent	33 percent
Temperature, T	93.33 ^{0}C	200 ^{0}F
Well radius, r_w	0.1 m	0.32 ft
Reservoir pressure, p_i	3.45×10^{7} Pa	5000 psia
Well pressure, p_{wf}	3.45×10^{6} Pa	500 psia

1.5 Validation

Currently, there are no analytical solutions for describing the complex shale physics and high nonlinearities associated with flow through these ultralow permeability reservoirs. In this section, we compare the rate and cumulative production forecasts from TAMSIM (Freeman, 2010), the unconventional gas reservoir simulator used in this research, with the forecasts made using the numerical model available in KAPPA (Ecrin product suite 2010), a which is a commercial software package for shale/tight gas analysis.

All simulations performed in this work were generated based on the assumption of single-phase gas flow (we expect to have water at or very close to residual water saturation). In these nanoporosity and ultra-low permeability shale-gas systems, the water in the matrix can be assumed to be practically immobile. Thus, the single-phase (gas) flow assumption may not have any significant effect on the results of this research.

To conduct this portion of the study, a multiply-fractured horizontal well with ten fractures was modeled using both simulators. Figure 1.1 shows a comparison of the gas rate forecast from TAMSIM to that obtained using Topaze, while Figure 1.2 gives the corresponding cumulative gas production estimates. Both plots show a near-perfect match with the results from Ecrin after 1 hour, and this serves as a validation of the correctness of TAMSIM. The awkward pattern of the rate forecasts from Ecrin at early times is most likely a numerical artifact, probably due to the approximate representations of the very minute fractures with much larger grid cells without the corresponding porosity modification discussed in Section 4.2. However, it is important to observe that the duration of this deviation (3.6 seconds to 1 hour) is much too short to have any significant effect on the cumulative production as seen in Figure 1.2.

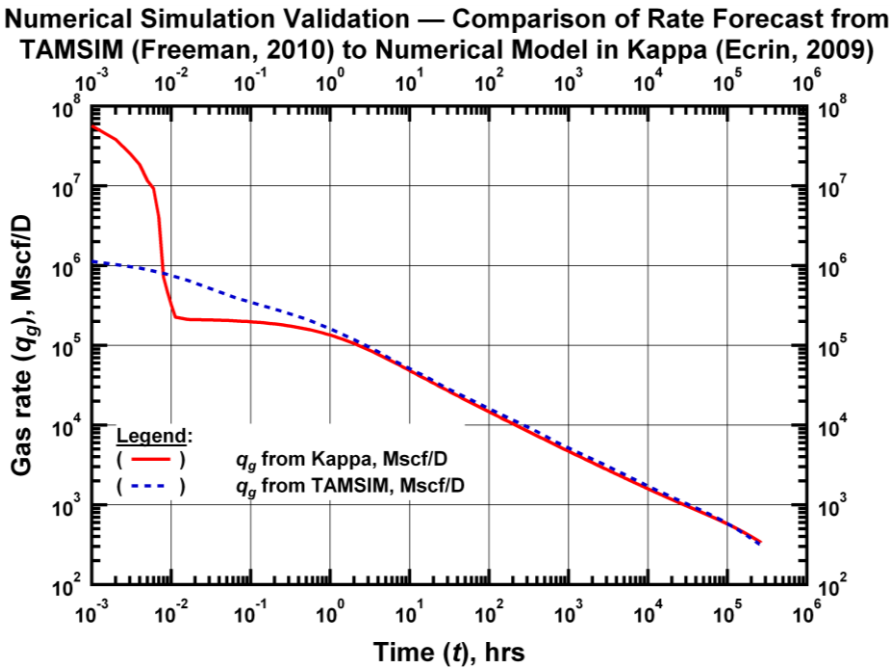

Figure 1.1—A comparison of the gas rate forecast from TAMSIM with that from Ecrin shows a good match.

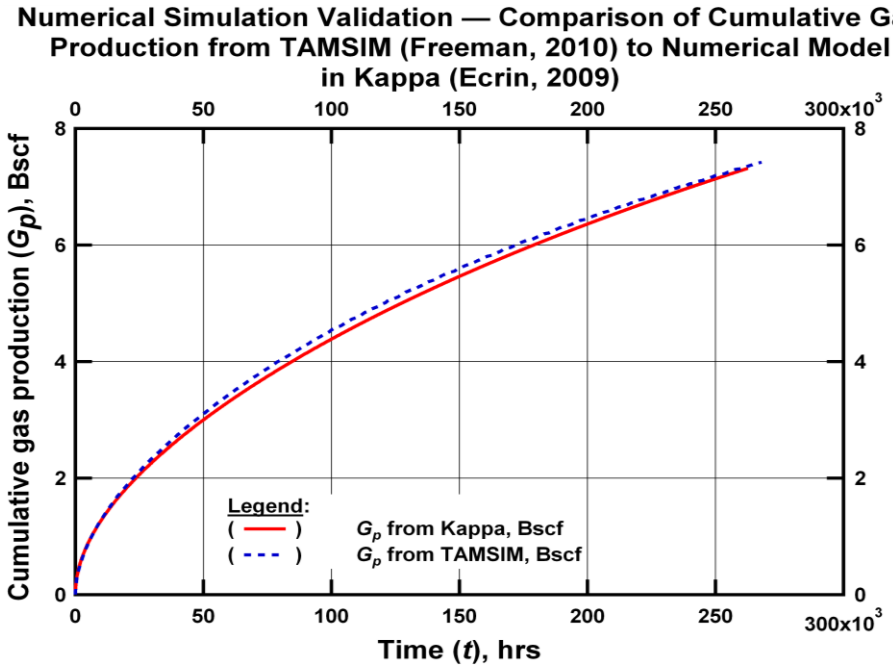

Figure 1.2—A comparison of the cumulative gas production forecast from TAMSIM with that from Ecrin (2010) shows a good match.

1.6 Research Overview

In this work we developed TAMMESH, a 3D Voronoi mesh-maker that uses the voro++ library to generate unstructured grid meshes. This mesh-maker does all the required pre-processing, while the actual simulations are performed using TAMSIM, an unconventional-gas reservoir simulator developed at Texas A&M University (Freeman et al., 2010). Our approach is to provide very high-definition reference numerical solutions that illustrate virtually all of the trends we can expect in an unconventional gas reservoirs. The grid-block dimensions vary from about 1 mm at the fractures to 50 m in the un-stimulated reservoir volume.

The specific cases studied in this work include the evaluation of the interaction between secondary and hydraulic fractures, the study of the effects of non-planar and non-orthogonal fracture geometries, and the assessment of the effect of representing a multiply-fractured horizontal well system with a single fracture or a repetitive element. Distinct production signatures using log-log and square-root plots are indentified and discussed.

CHAPTER II
LITERATURE REVIEW

This chapter gives an overview of the present status of the problem investigated in this research, and also provides the relevant theoretical background. We provide a brief survey of previous models to predict reservoir performance, we also discuss the use of Voronoi grids in reservoir simulation, and we illustrate different geometrical configurations and classifications of fractured shale-gas or tight-gas systems. We close this chapter with a discussion of the diagnostic plots that are used in this research.

2.1 Models for Predicting Reservoir Performance

Various analytical and semi-analytical solutions have been proposed to model flow in shale-gas and tight-gas reservoirs. Gringarten (1971) and Gringarten et al., (1974) developed some of the early analytical models for flow through domains involving a single vertical fracture and a single horizontal fracture, while more accurate semi-analytical models for single vertical fractures were developed much later (Blasingame and Poe Jr., 1993). Prior to the development of models for multiply-fractured horizontal wells (Medeiros et al., 2006), it was common practice to represent these multiple fractures with an equivalent single fracture, as shown in Section 3.2.1.

Several other analytical and semi-analytical models have been developed since Bello and Wattenbarger (2008); Mattar (2008); Anderson et al., (2010). Although these models are much faster than numerical simulators, they generally cannot accurately handle the very highly nonlinear aspects of shale-gas and tight-gas reservoirs because these analytical solutions address the nonlinearity in gas viscosity, compressibility and compressibility factor with the use of pseudo-pressures (an integral function of pressure, viscosity and compressibility factor) rather than solving the real-gas flow equation. Other limitations include the difficulty in accurately capturing gas desorption from the matrix, multiphase flow, unconsolidation, and several non-ideal and complex fracture networks (Houze et al., 2010).

The limitations of the analytical and semi-analytical models have led to the use of numerical reservoir simulators to study the reservoir performance of these unconventional gas reservoirs. Miller et al., (2010) and Jayakumar et al., (2011) showed the application of numerical simulation to history-matching and forecasting production from two different shale-gas fields, while Cipolla et al., (2009), Freeman et al., (2009), and Moridis et al., (2010) conducted numerical sensitivity studies to identify the most important mechanisms and factors that affect shale-gas reservoir performance. These numerical studies show that the characteristics and properties of the fractured system play a dominant role in the reservoir performance. Hence, significant effort needs to be invested in the characterization and representation of the fractured system.

Despite the large and expanding use of numerical simulation in the study of shale-gas and tight-gas reservoirs, large knowledge gaps remain. Very little is known about the interaction between primary and secondary fractures, as well as the effect of non-orthogonal and non-planar fracture orientations on the flow behavior of these unconventional gas plays. The reader is referred to Section 2.4 for a definition of each of these fracture classifications and orientations.

The goal in this work is to expand the current understanding of flow behavior in fracture systems involving the non-ideal fracture geometries that are typically encountered in field scenarios, and to provide information that can be used to:

(a) optimize fracture and completion design,
(b) validate analytical models, and
(c) allow more accurate reserves estimation.

2.2 Use of Voronoi Grids in Reservoir Simulation

The traditional approach of modeling fractured shale-gas reservoirs with regular Cartesian grids could be limited in that it cannot efficiently represent complex geologies, including non-planar and non-orthogonal fractures, and cannot adequately capture the elliptical flow geometries expected around the fracture tips in such fractured reservoirs. It also suffers from the fact that the number of grids can easily grow into millions because of the inability to change the orientation and shape of the grids away from the fracture tips, thus requiring extremely fine discretization in an attempt to describe all possible configurations. This problem is also aggravated by the large number (up to 60) of hydraulic fractures in a clustered fracture system (Jayakumar et al., 2011).

In this research, we have developed a mesh-maker that uses the voro++ library (Rycroft, 2007) to construct Voronoi or Perpendicular Bisector (PEBI) grids (Palagi and Aziz, 1994), which are sufficiently flexible to honor any geological complexities, and can assume any shape, size or orientation. The mesh-maker is used to grid all the ideal and non-ideal fracture geometries investigated in this study, and the actual simulation is performed using TAMSIM. The simulation results are then analyzed in search of distinctive production signatures, which can be useful in predicting production performance and flow regimes in these unconventional gas reservoirs.

2.3 Classification of Fractured Systems

Moridis et al. (2010) identified the distinct fracture systems present in producing shale-gas and tight-gas reservoirs. Figure 2.1 shows a graphical illustration of the four fracture systems, which are discussed below:

- **Primary or hydraulic fractures:** These are fractures that are typically created by injecting hydro-fracturing fluids (with or without proppants) into the formation. Proppants provide high-permeability flow paths that allow gas to flow more easily from the formation matrix into the well.
- **Secondary fractures:** These fractures are termed "secondary" because they are induced as a result of changes in the geomechanical status of a rock when the primary fractures are being created. Microseismic fracture mappings suggest that they generally intersect the primary fractures, either orthogonally or at an angle. Most prior studies assumed ideal configurations with orthogonal and planar fracture intersections so as to simplify the gridding; but in this work, we have developed an unstructured mesh-maker that facilitates the gridding of non-orthogonal, non-planar and other non-ideal fracture geometries.
- **Natural fractures:** As the name implies, these fractures are native to the formation in the original state, prior to any well completion or fracturing process.
- **Radial fractures:** These are fractures that are created as a result of stress releases in the immediate neighborhood of the horizontal well.

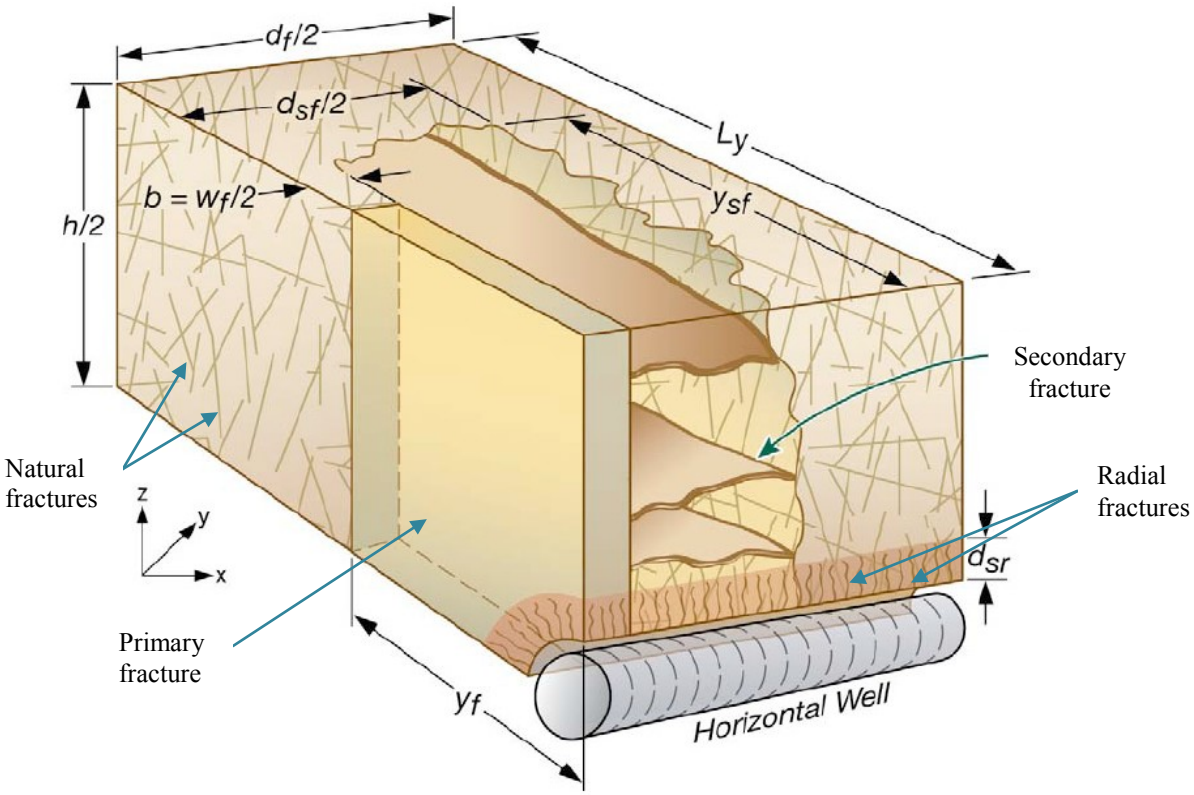

Figure 2.1—Identification of the four fractured systems (Moridis et al., 2010).

2.4 Illustration of Possible Fracture Geometries/Orientation

Houze et al., (2010) recognized the importance of explicitly gridding secondary fractures so as to quantify the interaction between primary and secondary networks as distinct systems, using either a regular orthogonal pattern or a more random and complex system. In this work, we have identified two classes of possible fracture geometries/orientations:

- **Regular or ideal fractures:** These are idealized fracture geometries, which are usually planar and orthogonal. A perfectly planar (or orthogonal fracture) is the idealized geometry used in numerical studies using Cartesian grids. Figure 2.2A gives an illustration of this fracture geometry.
- **Irregular or non-ideal fractures:** These are the kinds of fracture geometries we are likely to encounter in real-life. They could be non-orthogonal, meaning that the fractures intersect either the well (for primary fractures) or primary fractures (for secondary fractures) at angles other than 90^o, and they could be complex, meaning that the fractures are not restricted to a flat, non-undulating plane. Figures 2.2B and 2.2C give a diagrammatic illustration of two such scenarios.

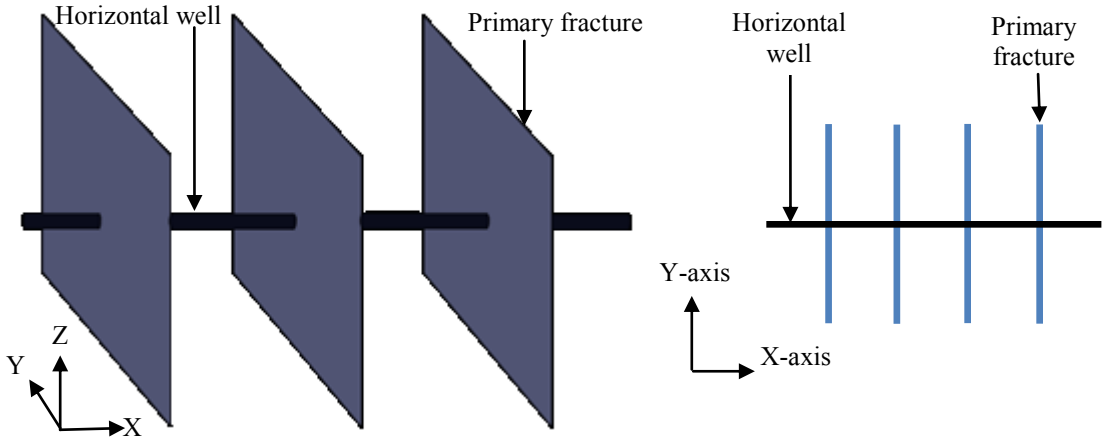

Figure 2.2A—3D and 2D plan views of planar orthogonal fractures.

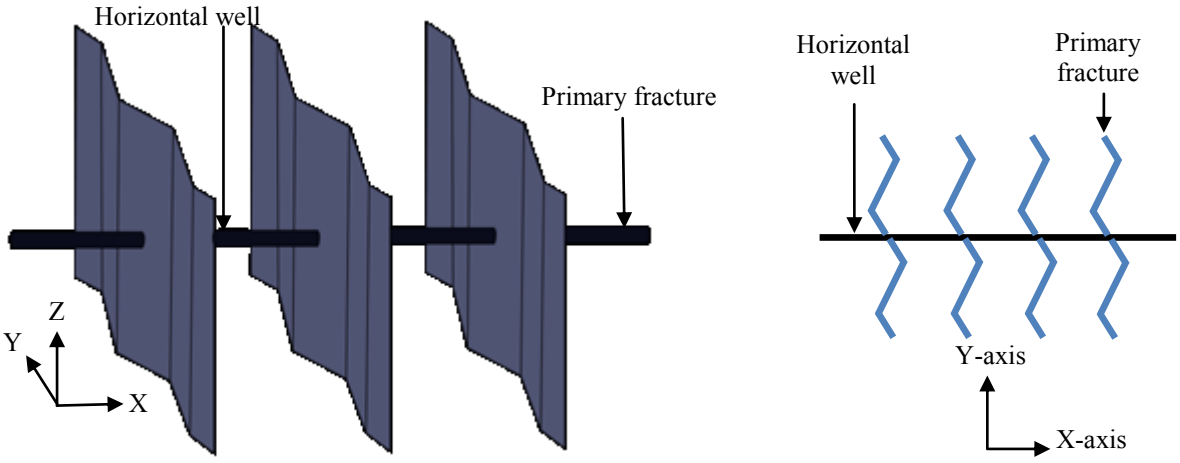

Figure 2.2B—3D and 2D plan views of non-planar fractures.

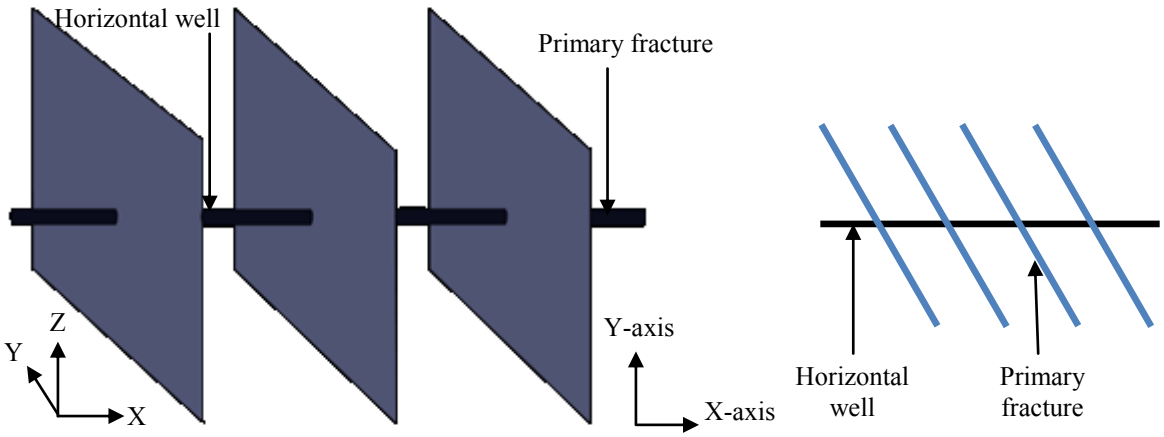

Figure 2.2C—3D and 2D plan views of non-orthogonal fractures.

2.5 Diagnostic Plots

Gas production can be analyzed using log-log plots of rate or dimensionless rate versus time or dimensionless time, plots of inverse of normalized rates versus square root-time (called square-root plots), flowing material-balance plots, dimensionless plots, rate derivative plots, rate-integral plots and rate-integral derivative plots, among others. Anderson et al. (2010) points out that the first three are particularly well suited for tight-gas and shale-gas production analyses.

In this research, we provide square-root plots, log-log rate (q) versus time (t) plots, and log-log plots of dimensionless rate (q_D) versus dimensionless time (t_D). The log-log plots show the different flow regimes exhibited by the reservoir, while the square-root plot indicates the size of the "stimulated reservoir volume" (SRV) during linear flow. The dimensionless variables are as defined below:

$$q_D = 141.2\frac{q\mu}{kh(p_i - p_{wf})} \quad \text{..... 2.1}$$

$$t_D = 0.0002637\frac{kt}{\phi\mu c_t x_f^2} \quad \text{..... 2.2}$$

where,

μ is viscosity in cp,

q is gas flow rate in *reservoir* cu ft

k is the matrix permeability in md

h is the reservoir thickness in ft,

p_i is the initial reservoir pressure in psia

p_{wf} is the flowing bottomhole pressure in psia

t is time in hours

ϕ is porosity as a fraction

c_t is total compressibility in psi^{-1}

x_f is the fracture half-length in ft

q_D and t_D are the dimensionless rate and time respectively

CHAPTER III
GENERATION OF UNSTRUCTURED GRIDS

This chapter describes the algorithm used in TAMMESH, that is, the unstructured mesh-maker that was developed as part of this research. Relevant portions of the C++ code are included to illustrate how cell centers are placed in a pattern that yields the desired geometry when the appropriate Voronoi gridding library call is invoked. The "voro++" (Rycroft, 2007) Voronoi library is used in this work to provide the Voronoi tessellations that yield the Voronoi or "perpendicular bisector" (PEBI) grids, using the cell centers that have been computed in TAMMESH.

In addition to the construction of grids, TAMMESH provides some pre-processing features. It facilitates the identification of the medium types (*i.e.*, lithology) of each grid-block, and also simplifies the representation of pressure-constrained internal boundaries, such as sources and sinks (wells) with highly-refined grid-blocks that have their porosities, permeabilities, pressures and temperatures set to values that are representative of the well conditions.

TAMMESH takes advantage of the Object-Oriented Programming and dynamic memory allocation features available in C++. It uses different methods for handling specific tasks, while the "main" method co-ordinates the program flow. All arrays were allocated dynamically using pointers for efficient memory management, particularly in the processing of the grid-block connections. Contrary to what occurs in regular Cartesian, tetrahedral or hexahedral meshes, each of TAMMESH grid-blocks can have a different number of neighbors.

3.1 Description of Gridding Algorithm

In this section, we provide a detailed explanation of some code snippets that are critical to the development of TAMMESH, the Voronoi mesh-maker used in this study. A high-level list of tasks to be completed in the gridding process is outlined below:

(a) Create an array of logarithmically-spaced points to be used for progressively coarsening the grid as we move away from the fracture faces and tips.

(b) Call the routine that constructs the grid by an iterative process applied to each layer and each fracture in a multiply-fractured horizontal well with multistage fractures.

(c) In the gridding routine, vary the X, Y and Z values incrementally, using the array of points discussed in (a). The algorithm used to vary the X, Y and Z values determines the fracture geometry that will be generated when the appropriate voro++ routine is called. These X, Y and Z values are parsed in as the arguments of the function call.

(d) Finally, extract the cell centers and volumes, connection areas, surface distances, angle of inclination between neighboring grid-blocks, and proceed to perform any desired preprocessing.

3.1.1 Code snippet for determining logarithmic spacing

The C++ code listing given in Figure 3.1 is used to compute the logarithmically-spaced set of points which is stored in the "pt" array. The placement of points in the simulation domain using this array results in a coarser discretization with an increasing distance from the fracture faces and tips. The logarithmic spacing is computed using the geometric series given below:

$$\Delta r_{i+1} = \Delta r_i \times f \quad \text{..... 3.1}$$

where:

Δr_i is the previous value of the increment to the position of the cell center. When $i = 0$, this value is the reference or initial increment, and it should be set to the fracture aperture.

Δr_{i+1} is the new increment to be added to the current position of a cell center.

f is a factor (greater than 1) that determines the rate at which the value of Δr increases.

The entire code snippet is repeated for the logarithmic spacing from the wellbore, but with a "deltaR" (*i.e.* Δr) value which is equal to the wellbore radius, and the calculated points are stored in the "pt1" array. The code comments clearly show the various operations at specific sections or lines in the code.

```
   deltaR         = 0.003;  // 3mm fracture aparture
   factor         = 1.3;    // factor used in logarithmic spacing
  //Determining logarithmic spacing orthogonally away from fracture face
   pt[0] = deltaR;
   for(ilogSpacnNum=1; ilogSpacnNum<=max_nLogGrids; ilogSpacnNum++){
      deltaR = deltaR * factor;                       //update deltaR
      pt[ilogSpacnNum] = pt[ilogSpacnNum-1] + deltaR; //increment point array
      if(pt[ilogSpacnNum] >= ((x_max-x_min)/2.0)){
         break;                                       //exit loop
      }
   }
```

Figure 3.1 C++ code listing for computing the logarithmic spacing array.

3.1.2 Nested loop for making iterative calls to the gridding routine

The C++ code listing given in Figure 3.2 consists of two nested loops, from where the "gridOneFrac" routine is called iteratively for gridding each of the fractures in the multiple fracture system and each of the layers of the mesh. The gridding of each layer is performed in the inner "while" loop by incrementing the Z value, using the "pt1" array discussed in the previous section. In a similar manner, the gridding of each fracture in a multiple fracture system is performed in the outer "for" loop, where the X value is progressively set to each fracture's center. The last line of the code in Figure 3.2 shows how I compute

the center of each fracture, by incrementing the value of the X co-ordinate of the current fracture center (*i.e.,* CentreX) with a value equal to the fracture spacing, which is the distance between two fractures.

```
//for loop to place multiple fractures in multiply fractured horizontal wells
for(ifracNum=1;ifracNum<=numFracs;ifracNum++){
   //call "gridOneFrac" repeatedly for each layer & each frac
   gridOneFrac(CentreX, CentreY, CentreZ, fracHalfLength, pt, pt1);
   //for loop to place grid centres in all layers
   while(pt1[layerCount] < (z_max-z_min)){
      gridOneFrac(CentreX, CentreY, CentreZ+pt1[layerCount], fracHalfLength, pt, pt1);
   }
   CentreX = CentreX + fracSpacing;
}
```

Figure 3.2 C++ code listing for iteratively calling the gridding routine.

3.1.3 C++ routine for gridding each layer and each fracture stage

Figure 3.3 presents the actual mesh generated using the algorithm discussed in this section, while the C++ listing given in Figure 3.4 shows the three most important parts of the routine that is used to discretize the sub-domain corresponding to half of a planar multiply-fractured horizontal well. The first part shows the grid construction at the middle of the Y-axis, where the horizontal well is located, the second part shows the grid construction at other points along the Y-axis, while the third part of the routine employs basic trigonometric functions to place the points in a way that yields a circular mesh around the fracture tip when the voro++ method "con.put()" is called.

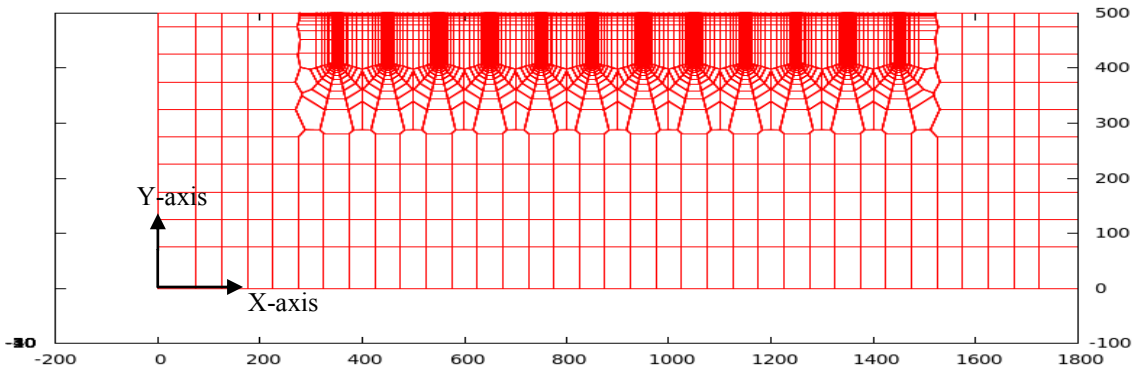

Figure 3.3—Ten multiple-fracture mesh generated using TAMMESH

```
void gridOneFrac(double CentreX, double CentreY, double CentreZ, double fracHalfLength,
                 double pt[], double pt1[]){
  //Gridding along the X axis at the middle of Y axis
  half_fracSpacing = (x_max - x_min) / (2.0*numFracs);
  for(j=0;j<ilogSpacnNum;j++){
     if(pt[j] >= half_fracSpacing) break;
     else {
        con.put(ElemNum,CentreX + pt[j],CentreY, CentreZ);
        con.put(ElemNum+1,CentreX - pt[j],CentreY, CentreZ);
        ElemNum += 2;
     }
  }
  //Gridding all other points along Y axis
   k = 0;
   while(pt1[k] <= fracHalfLength){
      incrmt =  pt1[k];
      Y = CentreY - incrmt;   // to do same thing symmetrically below Y axis
      con.put(ElemNum,CentreX, Y, CentreZ);  //gridding the fracture itself
      ++ElemNum;
      for(j=0;j<ilogSpacnNum;j++){
         if(pt[j] >= half_fracSpacing) break;
         else {
            con.put(ElemNum,CentreX + pt[j], Y, CentreZ);
            con.put(ElemNum+1,CentreX - pt[j], Y, CentreZ);
            ElemNum += 2;
         }
      }
      k++;
   }
   //Gridding the circular/elliptical region around fracture tip
   circCentreX = CentreX;
   circCentreY = CentreY - fracHalfLength;
   for(j=0;j<=6;j++){
      angle = double(-j*30.0);
      for(k=0;k<ilogSpacnNum;k++){
         X = circCentreX + pt[k]*cos(PI*angle/180.0);
         Y = circCentreY + pt[k]*sin(PI*angle/180.0);
         if(X >= (circCentreX + half_fracSpacing) || Y >= y_max || X <= (circCentreX -
            half_fracSpacing) || Y <= y_min) break;
         con.put(ElemNum,X,Y,CentreZ);
         ++ElemNum;
      }
   }
}//end of method
```

Figure 3.4 C++ routine for gridding each layer and fracture by making a voro++ library call.

3.2 Grid Description

This section gives a detailed description of all the grids that have been generated in this work. All grids were visualized using "Gnuplot", a free Unix software package that provides the flexibility of zooming in on specific regions of the grid, viewing grid centers, and also rotating grids to allow visualization from different perspectives.

The next five subsections show a detailed visualization of the grids we have constructed for:

- Single-fracture representation of multiply-fractured horizontal wells,
- Planar multiply-fractured horizontal wells,
- Non-planar multiply-fractured horizontal wells,
- Non-orthogonal multiply-fractured horizontal wells, and
- Secondary fracture networks.

3.2.1 Single-fracture representation of multiply-fractured horizontal wells

This section shows the grids that have been constructed for the representation of a multiply-fractured horizontal well with an equivalent single fracture. The single fracture is assigned a fracture half-length that is equal to the sum of all individual fracture half-lengths, as illustrated in Figure 3.5 (Houze et al. 2010).

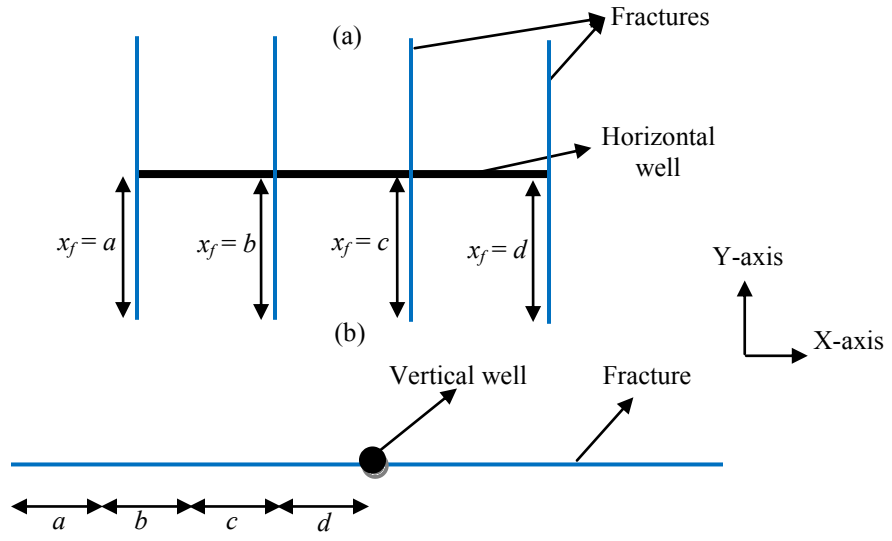

Figure 3.5—Schematic showing (a) a multiple-fracture case with four fractures and a half-length of x_f, and (b) the single fracture representation of this multiple fracture well with an apparent fracture half-length, $x_{mf} = a+b+c+d$ or $x_{mf} = n*x_f$ (where n is the number of fractures).

As discussed in Section 2.1, it was common practice to represent a multiply-fractured horizontal well system with an equivalent single fracture before the analytical models for these multiple fractures were developed. The analysis of the simulation results for the single-fracture representation of a multiple-fracture system is given in Section 4.1.

The length and breadth of the reservoir volume simulated in the single-fracture case was changed from 1800 m X 1000 m (in the actual multiple fracture case) to 800 m X 2250 m, so that we can represent a fracture half-length of 900 m and maintain the same reservoir volume.

Figure 3.6 shows a 3D view of the mesh for a single-fracture representation that was constructed using TAMMESH. In this figure, only half of the domain is modeled on the basis of symmetry about the (XY)-plane at Z = -50 m, but it is important to point out that for a 3D grid, we can have as many as three planes of symmetry:

(a) (XY)-plane, at the middle of the Z axis (i.e. Z = -50 m, since total thickness is 100 m),

(b) (XZ)-plane, at the middle of the Y axis, and

(c) (YZ)-plane, at the middle of the X axis.

This means we can model as little as one-eighth of a reservoir domain and multiply the rate forecasts by eight to obtain the production forecast for the full grid. The simulation of a fraction of the full grid reduces the number of grid-blocks and correspondingly reduces the size of the Jacobian matrix and the execution time. Figures 3.7(a) and (b) show the 2D plan view of the grid shown in Figure 3.6, while Figure 3.7(c) gives an expanded view of the circled mesh region shown in Figure 3.7(a).

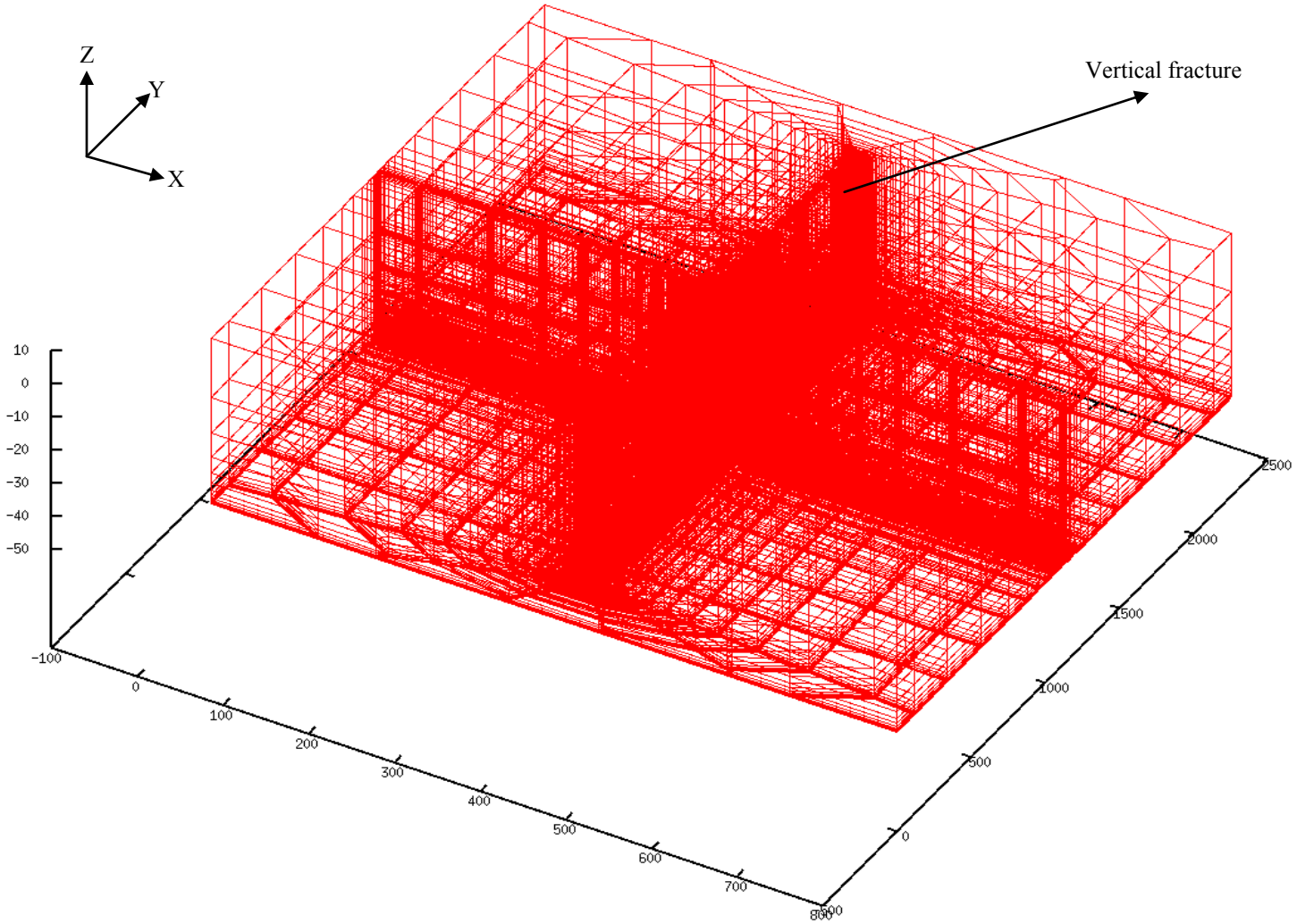

Figure 3.6—3D view of the single-fracture representation of a multiply-fractured horizontal well.

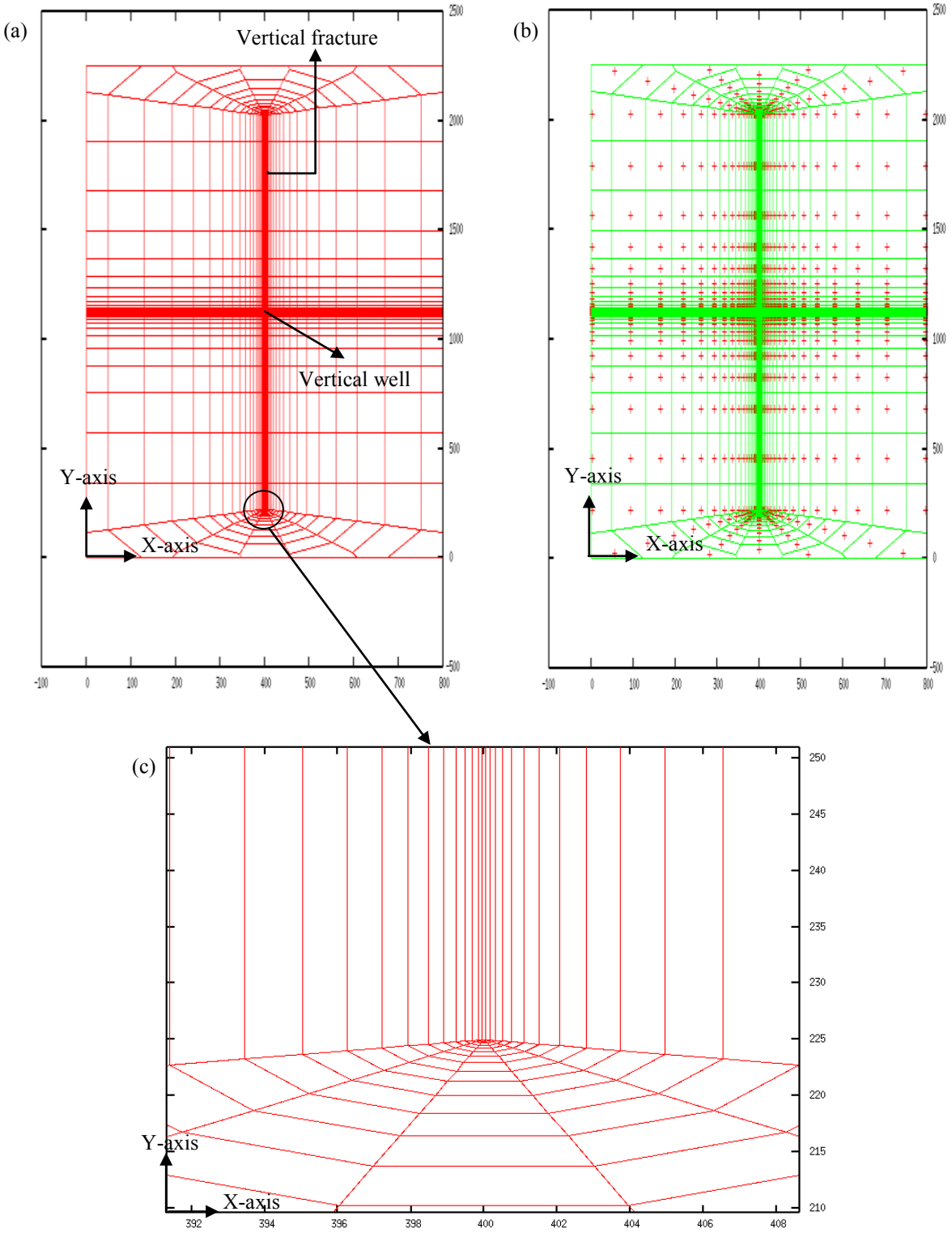

Figure 3.7 (a) Plan view of a single-fracture system; (b) Plan view with cell centers; and (c) Expanded view of the highlighted portion of the grid in (a).

3.2.2 Use of stencils for representing multiply-fractured horizontal wells

In this section, we discuss the use of a "minimum repetitve element", referred to as a "stencil", to represent a multiply-fractured horizontal well system. Freeman (2010) provides a schematic diagram and a discussion of the assumptions on which the use of stencils is based, and he uses this stencil for all the simulations he performed. Figure 3.8 gives the 2D plan view that shows the full multiple-fracture system (discussed in the next section) and illustrates the stencil in relation to the full system.

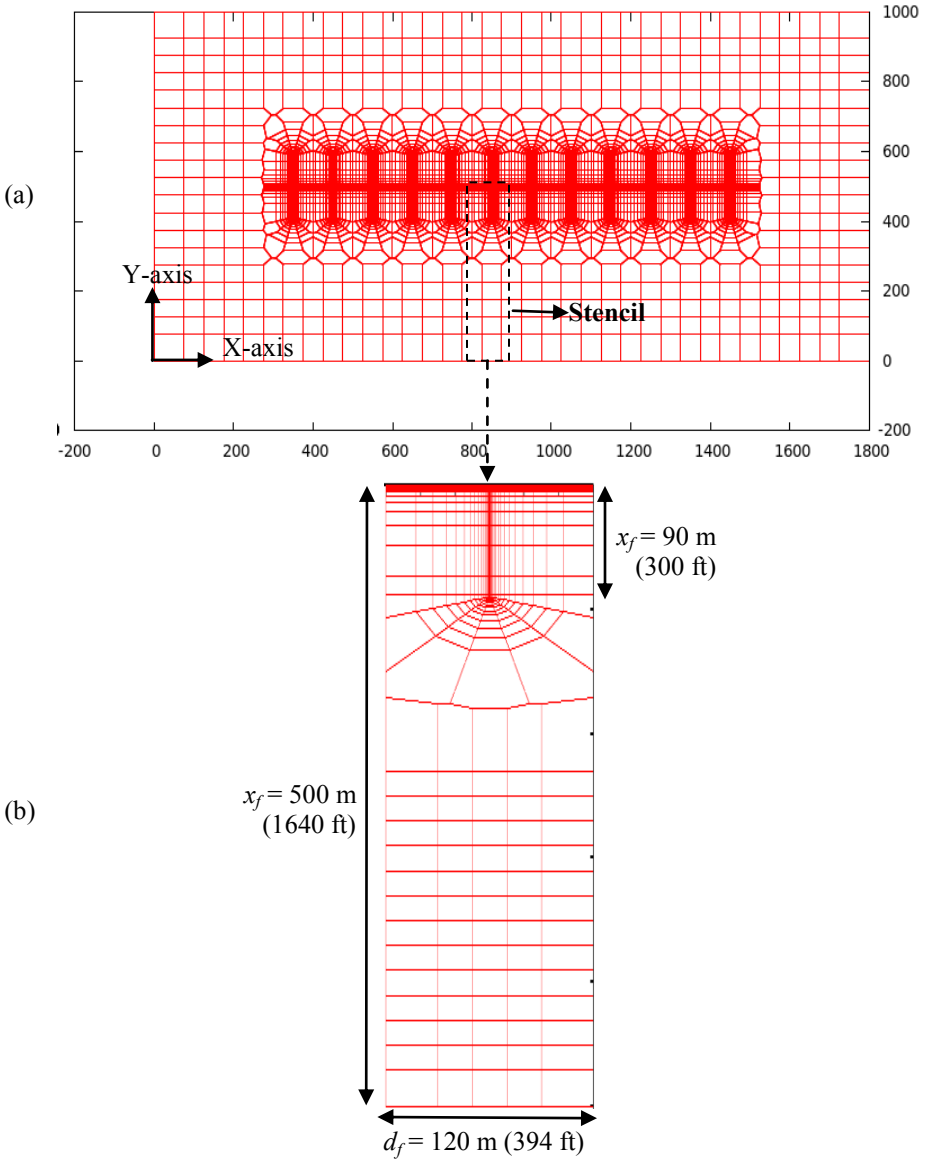

Figure 3.8—Plan view of grid shows (a) the full multiple-fracture system, and (b) the "minimum repetitive element" or "stencil".

In Section 4.2, we evaluate the accuracy of this approximation, which has the advantage of significantly reducing the problem size, since we simply model a stencil and multiply the rate and cumulative production by the number of times this minimum repetitive element occurs in the simulation domain.

3.2.3 Planar multiply-fractured horizontal wells

Figure 3.9 shows a plan view of the grid for both the stimulated and unstimulated reservoir volumes. The dotted line shows that there is a plane of symmetry about the (X,Z)-plane, at the middle of the Y-axis, which corresponds to Y = 500 m. This implies that only the region above or below the dotted line needs to be modeled, and then multiply the rate forecasts by a factor of two. It is important to note that the (Y,Z)-plane (not shown) is also a plane of symmetry about the X =900 m axis, meaning that the mesh can be halved again with no reduction in the quality of the predictions. We have included a "nonstimulated" region around the "stimulated reservoir volume" (SRV) to allow an elliptical flow from this region into the stimulated region, and finally into the wells. The 3D sketch corresponding to this planar system is shown in Figure 2.2A.

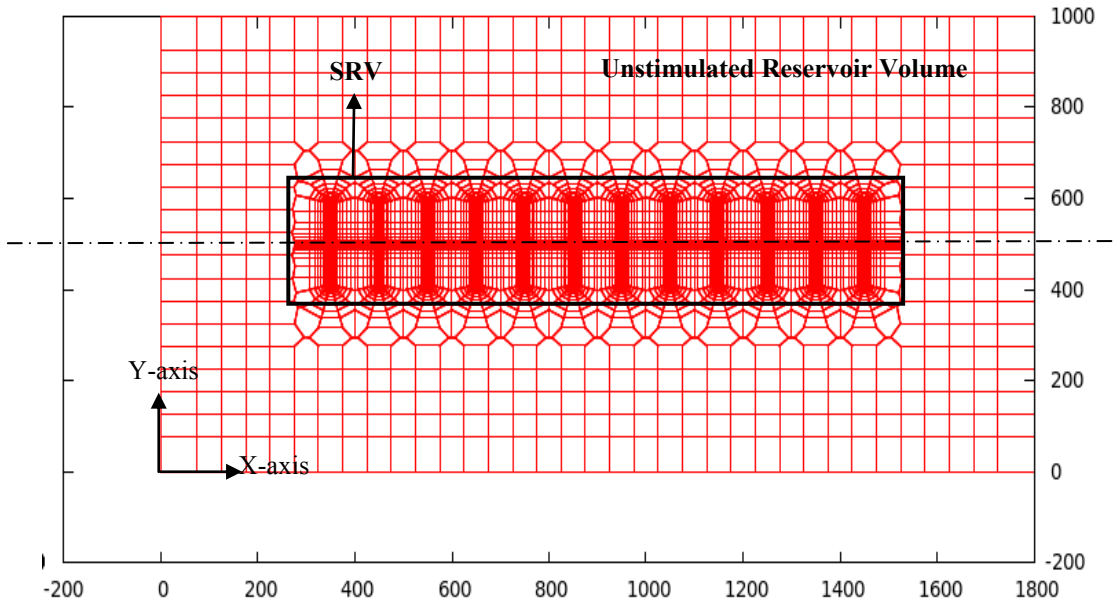

Figure 3.9—Plan view of multiply fractured horizontal well showing both the stimulated and unstimulated reservoir volume. Only half of the simulation domain is needed to be modeled because the reservoir is symmetric about the dotted line.

3.2.4 Non-planar multiply-fractured horizontal well systems

To grid a non-planar multiple-fracture system, the centers of the fracture cells are placed in a repeated pattern of equilateral triangles as illustrated in Figure 3.10. Since equilateral triangles have all 3 internal angles equal 60^o, we obtain "regular" hexagonal grid-blocks (a "regular" hexagon is a hexagon with equal sides and equal angles, while an "irregular" hexagon is one with unequal sides and unequal angles), which accurately represent fractures with an inclination angle of 60^o, when the Voronoi tessellation routine of the voro++ library is called. As explained by Palagi and Aziz (1994), the triangles which yield the Voronoi or PEBI grids after the Voronoi tessellation are referred to as the "Delaunay triangles". Figure 3.10 also shows how easy it is to change the fracture orientation with the use of these regular hexagonal cells.

A 3D schematic diagram of a non-planar multiple-fracture system appeared in Figure 2.2B. Figure 3.11(a) shows a plan view of the mesh generated using TAMMESH, while Figures 3.11(b) and 3.11(c) show progressively expanded views of the circled region in Figures 3.11(a) and 3.11(b), respectively.

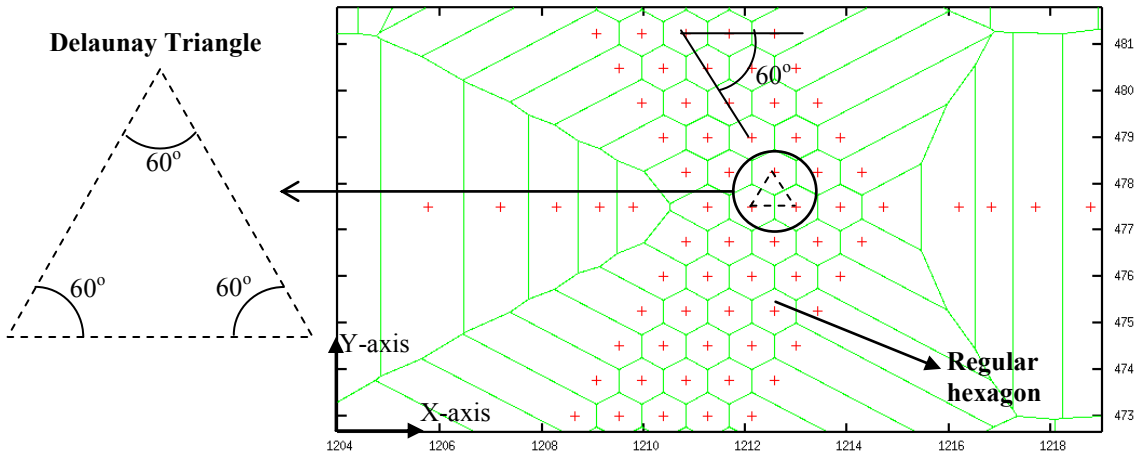

Figure 3.10—Expanded view of the region around the fractures shows that the placement of cell centers in the triangular pattern yields the desired 60^o fracture inclination angle.

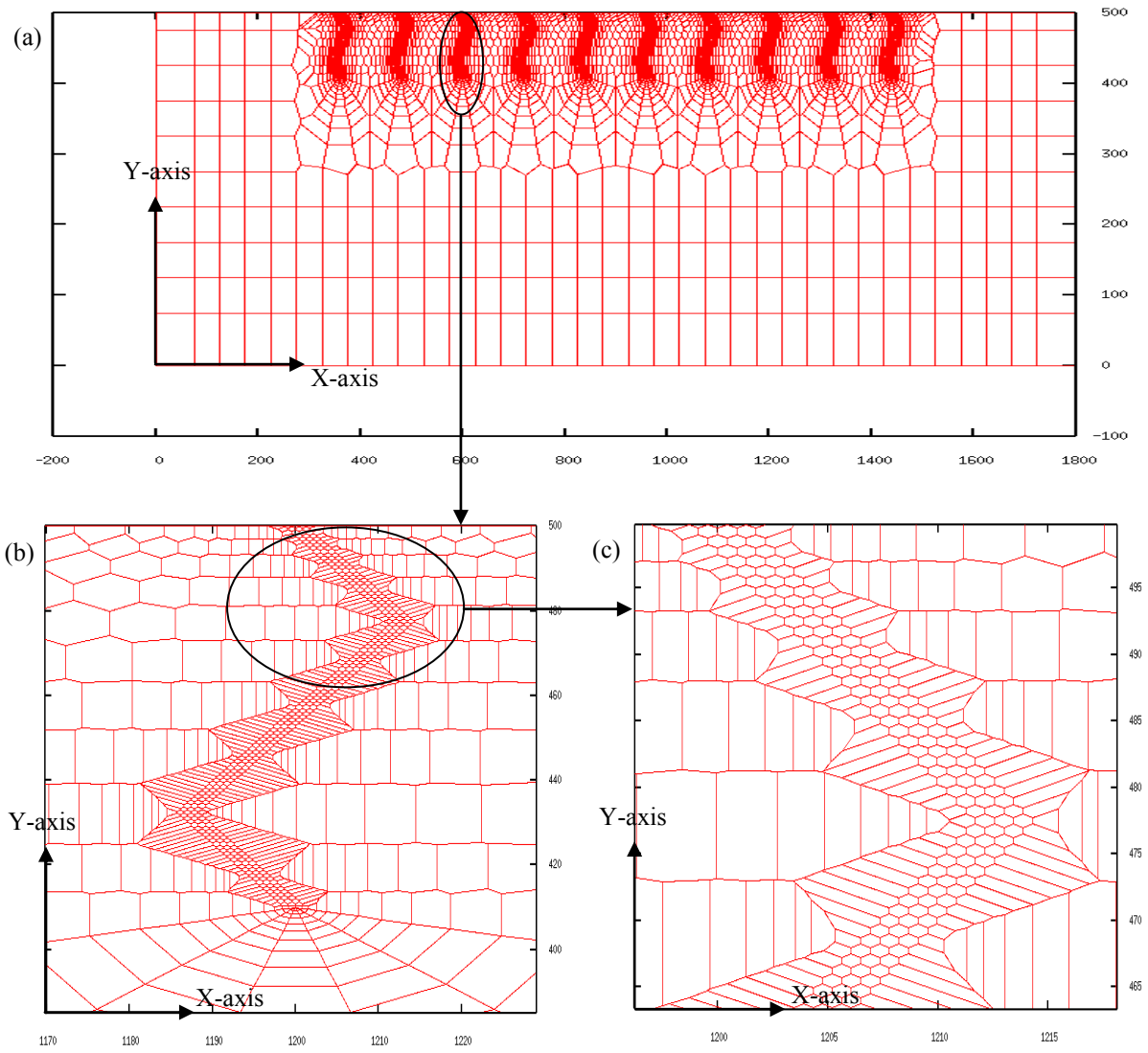

Figure 3.11 (a) Plan view of a non-planar fracture system; (b) An expanded view of the circled region in (a); (c) An expanded view of the highlighted portion of the grid in (b).

3.2.5 Non-orthogonal multiply-fractured horizontal wells

A description of a non-orthogonal fracture system is provided in Figure 2.2C. In this section, I model two different inclination angles ($\theta = 60^o$ and $\theta = 30^o$, respectively), defined as the angle between the fractures and the horizontal well. When $\theta = 60^o$, the cell centers are placed exactly as explained in Section 3.2.4, except that there is no need to change the orientation of the fractures because the fractures are planar in this case. Figure 3.12(a) gives a plan view of the grid constructed, while Figures 3.12(b) and 3.12(c) show progressively expanded views of the circled regions in Figures 3.12(a) and 3.12(b), respectively.

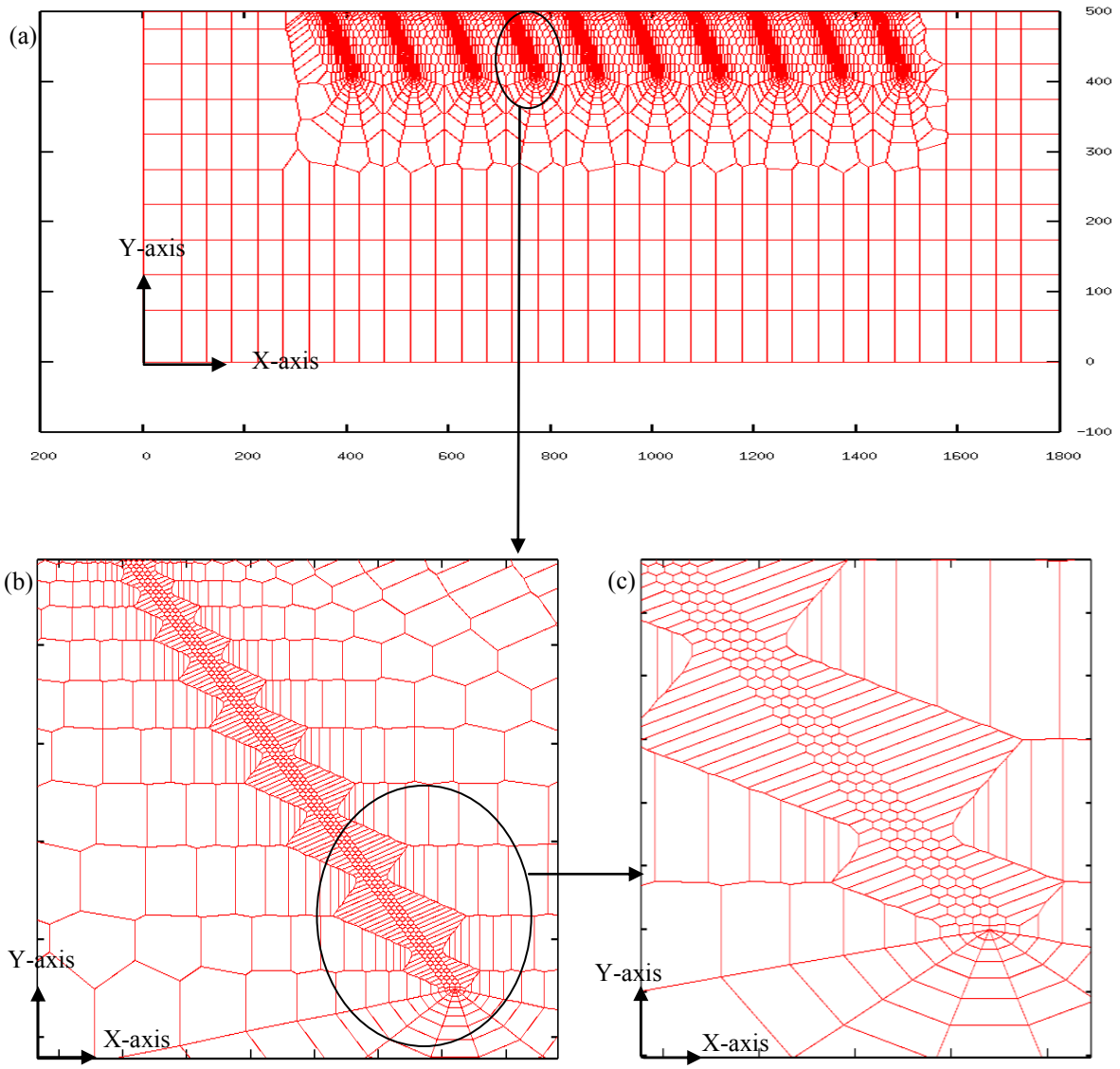

Figure 3.12 (a) Plan view of a non-orthogonal fracture system with $\theta = 60^{o}$; (b) An expanded view of the circled region in (a); (c) An expanded view of the highlighted portion of the grid in (b).

Figure 3.13 depicts the grid used for the simulation of a fractured system with non-orthogonal fractures that are inclined at an angle of 30^{o} from the horizontal well. In this case, the points are placed in the domain in a repeated pattern of isosceles triangles. Each triangle has its smallest angle set to 30^{o}, while the other two angles are equal, as shown in Figure 3.14. The appropriate Voronoi tessellation function of the voro++ library is called with the cell centers, and we obtain the desired irregular hexagonal grid-blocks, which provide the flexibility that is required to construct the grids for the non-orthogonal fractures with an inclination angle of 30^{o} to the horizontal well.

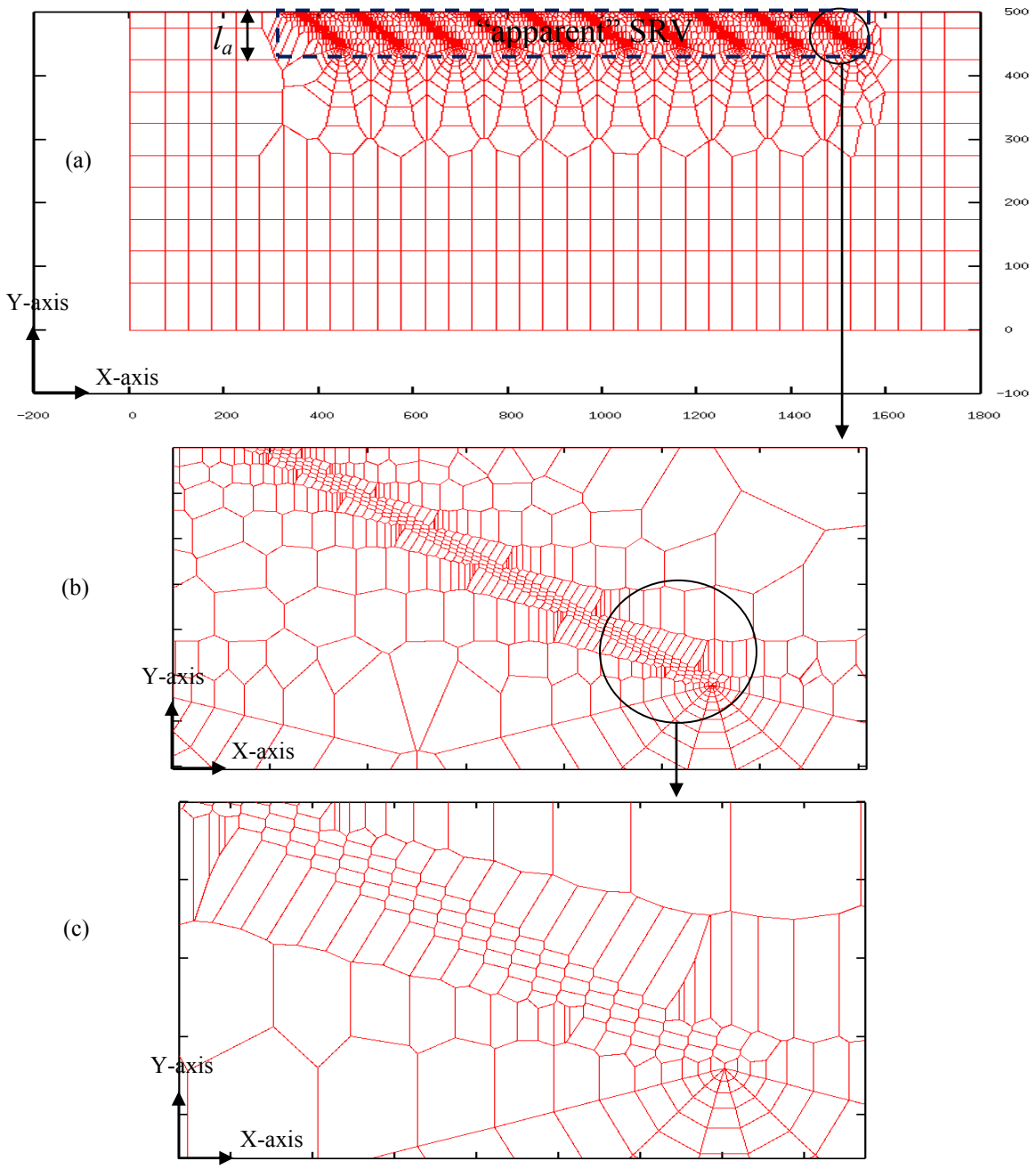

Figure 3.13 (a) Plan view of a non-orthogonal fracture system with $\theta = 30^{o}$; (b) An expanded view of the circled region in (a); (c) An expanded view of the highlighted portion of the grid in (b).

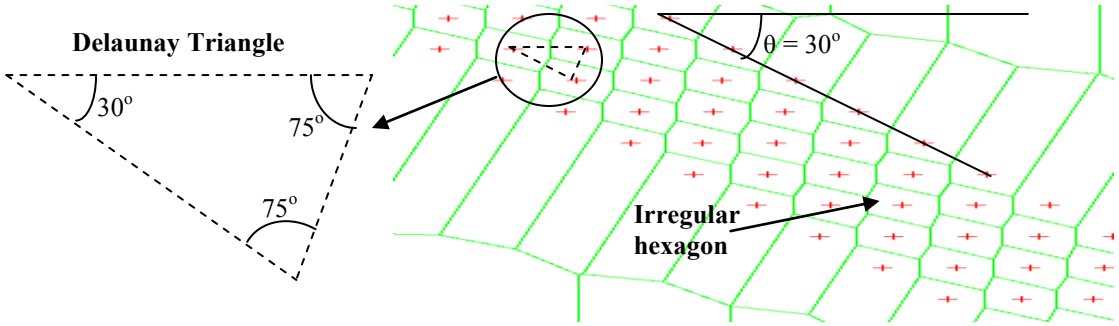

Figure 3.14—Expanded view of the region around the fractures shows that the placement of cell centers in the triangular pattern yields the desired 30° fracture inclination angle.

3.2.6 Secondary fracture networks

Three different configurations of induced secondary fractures are studied in this reserarch. The first case, illustrated by the schematic in Figure 3.15 shows a secondary fracture that intersects the primary fractures in the plane of the horizontal well, which is along the middle of the reservoir, in the Z-direction. In the second case, shown in Figure 3.16, the induced fracture intersects the primary fractures at $h/4$ from the top of the primary fracture, where h is the thickness of the reservoir. Finally, the last case illustrated in Figure 3.17 shows two induced fractures that intersect the primary fractures at $h/4$ and $3h/4$, repectively, from the top of the reservoir. For these secondary fracture systems, we use 3D grids that have been halved in the (X,Z)-plane of symmetry, at the middle of the Y-axis.

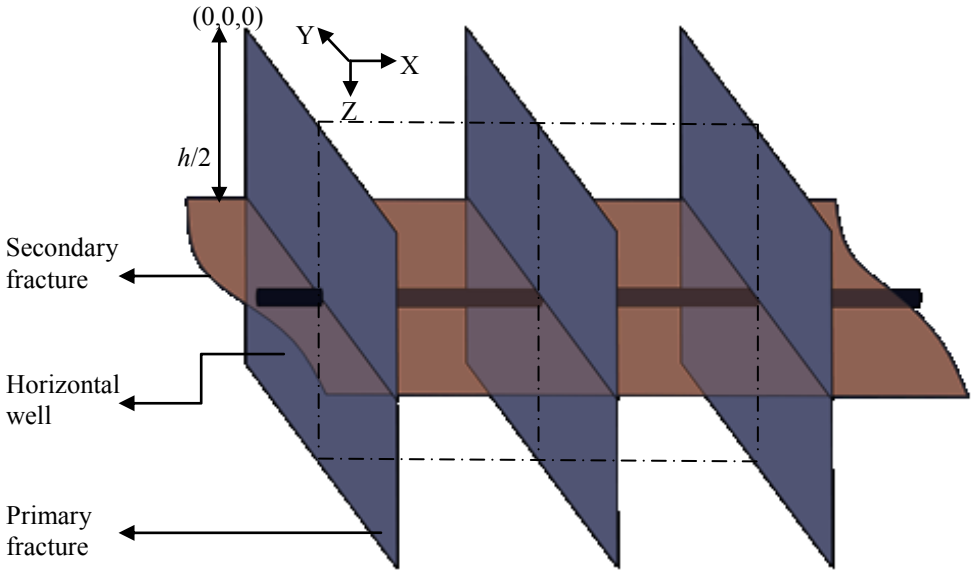

Figure 3.15—Schematic view of a secondary fracture middle layer of the reservoir. The dotted lines show the (X,Z)- plane of symmetry, at the middle of the Y-axis.

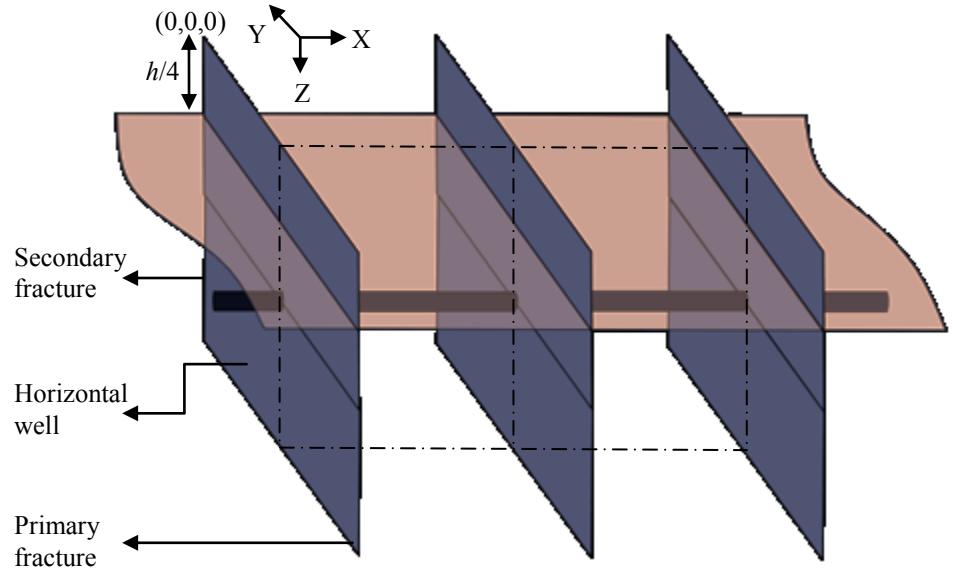

Figure 3.16—Schematic of a secondary fracture that intersects the primary fracture at, $h/4$ from the top of the primary fracture. The dotted lines show the (X,Z)-plane of symmetry, at the middle of the Y-axis.

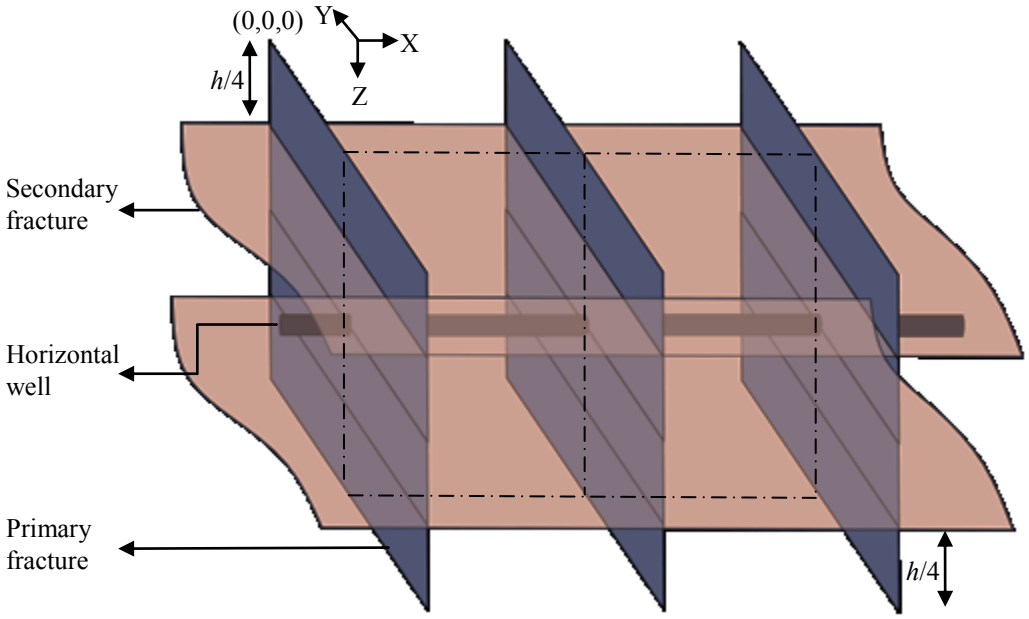

Figure 3.17—Schematic of two secondary fractures that intersect the primary fractures at $h/4$ and $3h/4$ from the top of the reservoir, respectively. The dotted lines show the (X,Z)-plane of symmetry, at the middle of the Y-axis.

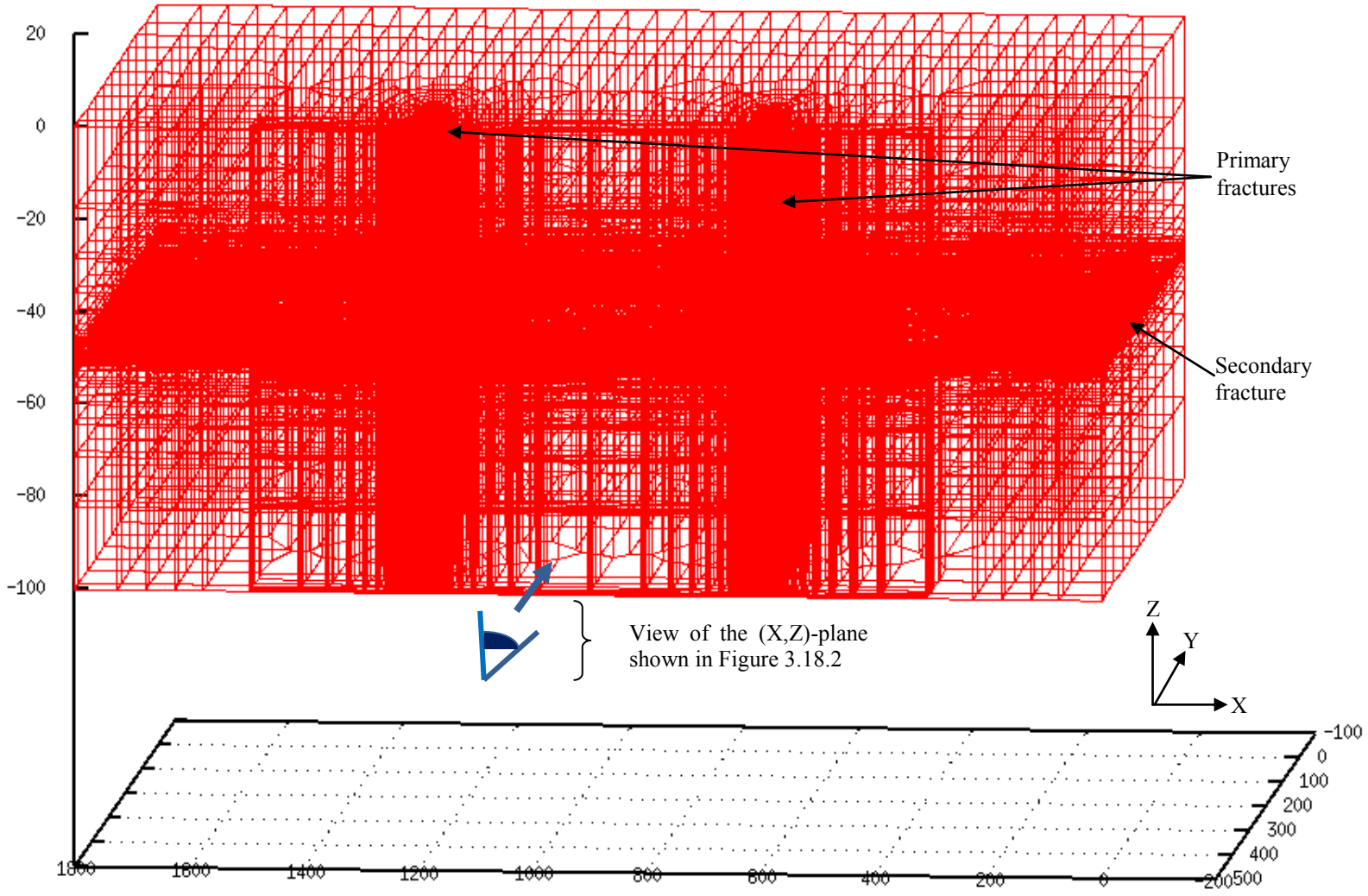

Figure 3.18—3D view of a centered secondary fracture intersecting two primary fractures.

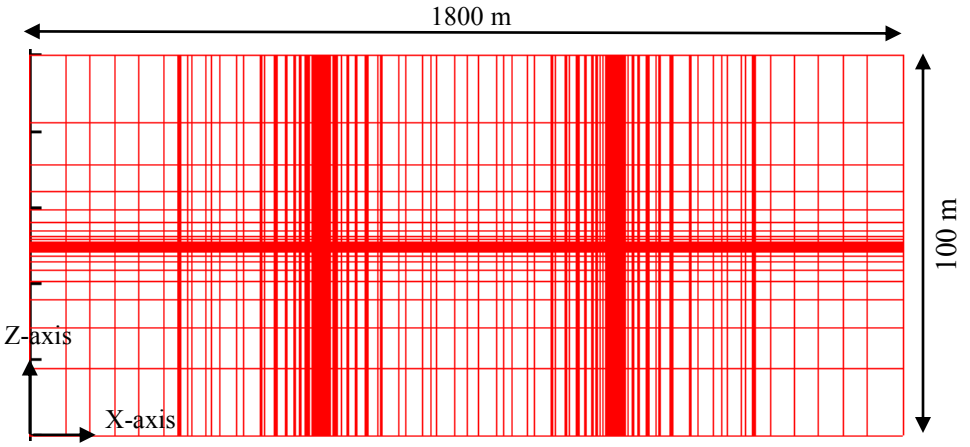

Figure 3.19—Side view (X-Z plane, at the middle of the Y-axis) of the mesh shown in 3.18 shows the logarithmic spacing, with discretization becoming coarser away from the fracture faces and wells.

Figure 3.18 gives a 3D view of the first case with two primary fractures only. The side view of this mesh, given in Figure 3.19 shows the logarithmic spacing of the layers away from the middle layer, where the horizontal well and the secondary fracture are located. In all cases, the fractures and wells are represented discretely, using grid-blocks with dimensions that are representative of the fracture aperture and well radius, respectively. The logarithmic spacing accurately captures the transient flow from the matrix into the fractures and wells, while minimizing the number of grid-blocks used in the simulation study.

3.3 Conclusions and Recommendations

The unstructured gridding technology provided in this work gives the capability and flexibility that is required to represent a variety of non-ideal fracture geometries and orientations. This chapter illustrates the gridding of primary and secondary fractures, as well as non-planar and non-orthogonal fracture orientations.

All grids shown in this chapter were constructed by explicitly placing points at desired locations in the simulation domain, using TAMMESH. A detailed discussion of the algorithms used to generate the grids for the different fracture geometries and orientations were provided. From the expanded views in Figures 3.6, 3.7 and 3.8, we observe that the change in the shape of the grid-blocks (from hexagonal to quadrilateral cells, in the non-planar and non-orthogonal fracture cases) does not appear smooth. A possible improvement in the gridding of these irregular fracture systems could involve the use of automatic adaptive gridding schemes, which are now getting more attention in the literature (Romain et al., 2011).

CHAPTER IV
SIMULATION RESULTS AND ANALYSES

This chapter presents the reservoir simulation results of this study and provides a discussion and interpretation of the findings, including identifiable trends and patterns.

4.1 Evaluation of Single-Fracture Representation of Multiply-Fractured Horizontal Wells

As discussed in Section 2.1, it was common practice to represent a multiply-fractured horizontal well system with an equivalent single fracture before the analytical models for these multiple fractures were developed. Section 3.2.1 gives a detailed discussion of this concept of single-fracture representation, and in this section, we seek to evaluate its accuracy.

Although well beyond the lifespan of most wells, the simulation in this section covered a production period of 3,000 years in order to show the different flow regimes that are expected in a multiply-fractured horizontal well system and in its single-fracture representation. We observe in Figure 4.1 that both approaches include a linear half-slope flow regime and a reservoir boundary-dominated flow. The very early-time fracture drainage observed before the onset of the linear half-slope line lasts a single day, and is insufficient to reach any conclusions about its behavior because it can be severely affected by numerical artifacts and discretization errors.

The log-log plot of the gas production rates given in Figure 4.1, shows that the single-fracture representation appears to be a good approximation because its rate forecast closely matches that of the multiply-fractured horizontal well system for any practical production timeframe. However, despite the fact that the "stimulated reservoir volume" (SRV) is the same in both cases, we observe that the multiple-fracture case begins to show fracture-interaction after about 20,000 days (55 years). The fracture-interference results in a reduction in slope, and the rate-profiles for the two cases cross after about 30 years. This fracture-interference is completely absent in the single-fracture case because it has just one hydraulic fracture, and it continues to exhibit linear flow until the true reservoir boundary is felt.

From the results, we can say that the single-fracture representation of multiple-fractures seems to give good results as long as we are in the linear flow regime, and this linear flow regime can last for up to 30 years. The duration of the linear flow regime is strongly dependent on the matrix permeability and fracture spacing. We also observe that the rate forecast for the multiple-fracture case is slightly more than that for its single-fracture representation before the onset of fracture interference, and this difference may be as a result of additional flow towards more fracture tips (Houze et al., 2010) or just a numerical artifact.

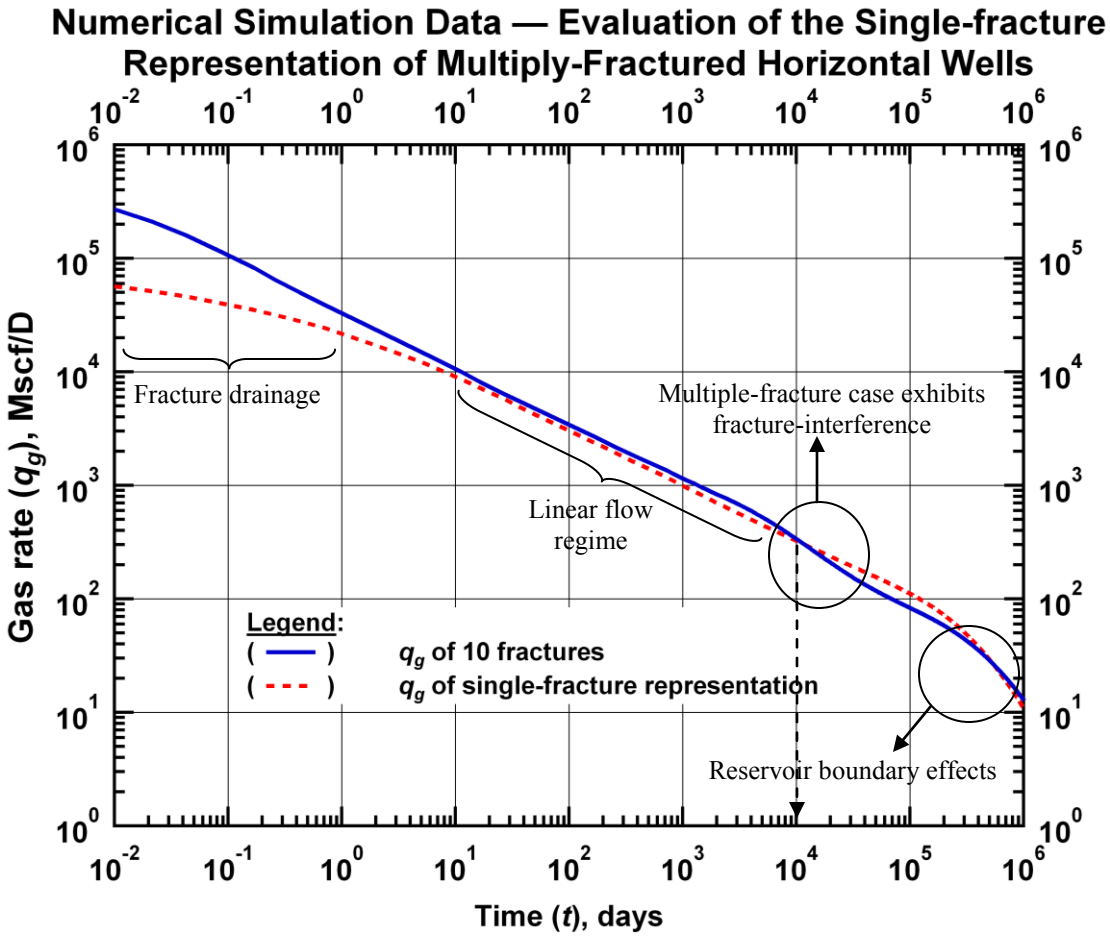

Figure 4.1—Comparison of a single-fracture representation with the actual multiple fractures shows absence of fracture interference in the former.

Figure 4.2 gives the cumulative production plots for both the multiple-fracture and single-fracture systems. We observe that, given the significant uncertainties in the estimation of flow parameters, the production rate forecast for the two fracture systems practically coincide. Significant deviations appear to occur at times that are orders of magnitude larger than any normal well operation period, and this deviations could be consequent on the onset fracture-interference in the multiple-fracture system, which is absent in the single-fracture case.

(a)

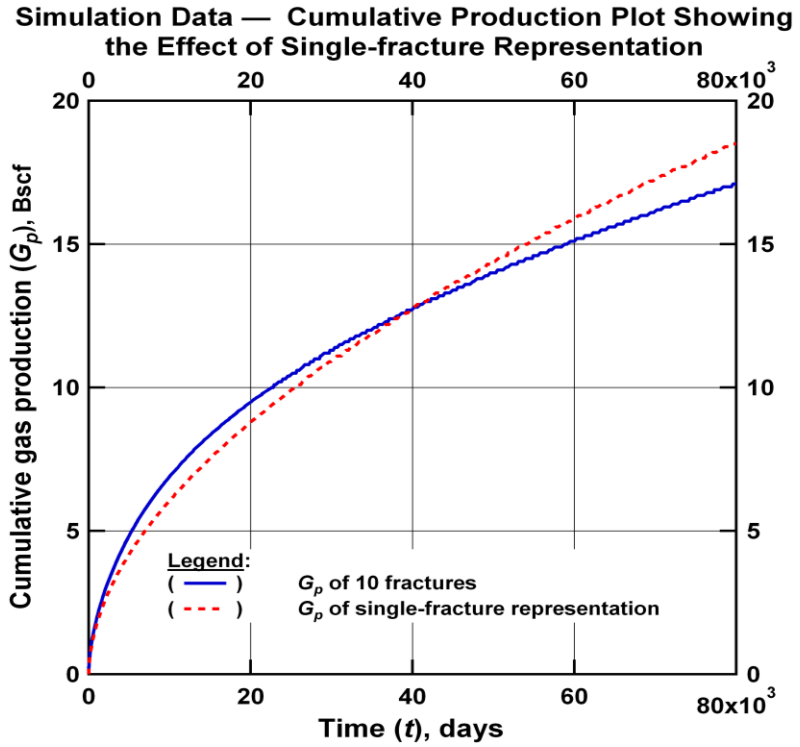

(b)

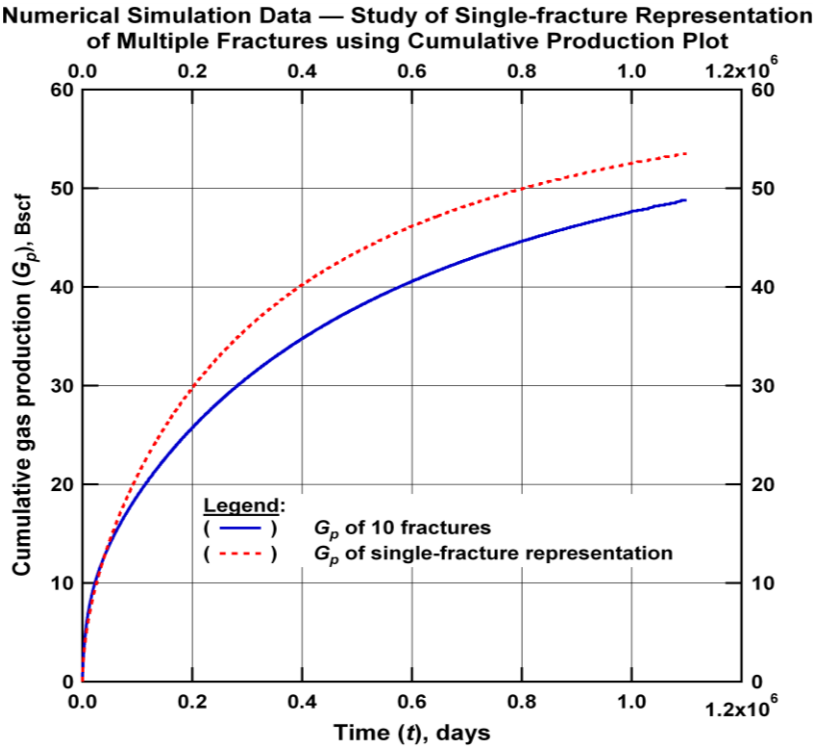

Figure 4.2—Cumulative production plots after (a) 220 years and (b) 3,000 years show that the single-fracture representation initially gives slightly lower production, but later gives more production than the multiple-fracture case.

(a)

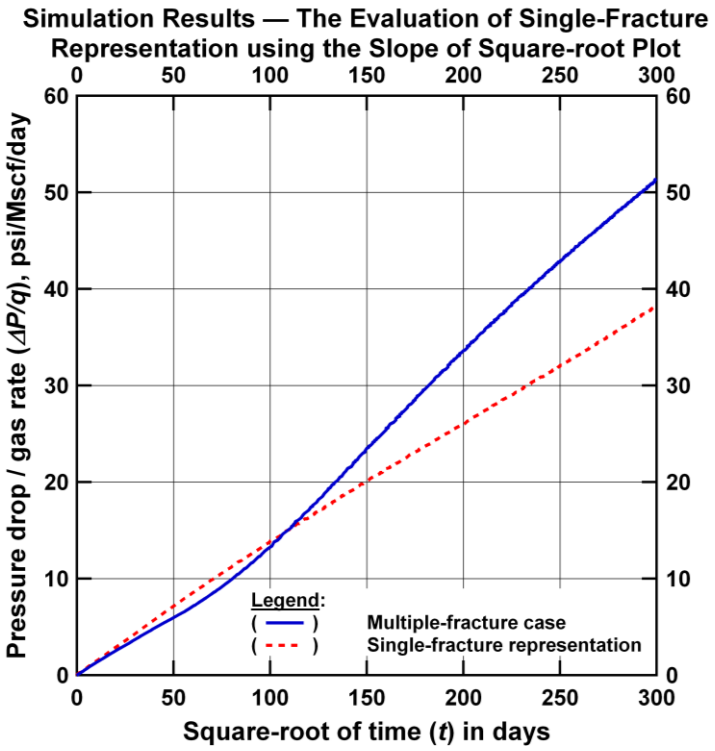

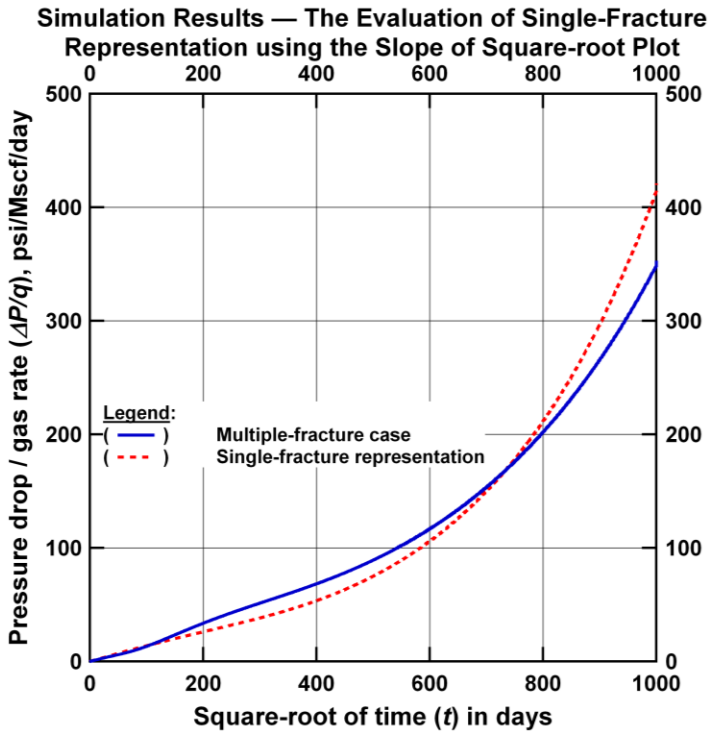

Figure 4.3—Square-root plots after (a) 250 years and (b) 3,000 years show that the single-fracture representation has a slightly higher value of slope when the square-root of time is less than 70 (about 13 years).

The square-root plots of both the multiple-fracture and its equivalent single-fracture representation are given in Figure 4.3. The square-root plot is generally used for estimating the Linear Flow Parameter (LFP = $A\sqrt{k}$) when the reservoir is in the linear flow regime (Anderson et al., 2008). We can say that the area of the SRV increases as the slope of the square-root plot decreases because the LFP is inversely proportional to the slope of a square-root plot and the matrix permeability is invariant. Figures 4.3(a) and (b) show that the area of the SRV in the multiple-fracture case is slightly higher than that of the single-fracture case, and this is in line with the slightly higher rates seen in the linear flow-regime (Figure 4.1). As observed with the flow profiles, the square-root plot for the single-fracture system does not show any significant deviation from that of the multiple-fracture system during normal production life (less than 30 years).

Furthermore, we observe from Figure 4.3(a) that the slope of the multiple-fracture square-root plot changes before that of its single-fracture representation. This is expected because the multiple-fracture system transitions into the fracture-interaction period (confirmed by the drop in the half-slope in Figure 4.1), but the single-fracture case does not show this flow behavior.

Figure 4.4 presents a high-resolution visualization of the pressure profiles for a multiply-fractured system, obtained using "Paraview", a free scientific visualization software package. Figure 4.4(a) and (b) confirm the linear flow from the low-permeability matrix into the high-permeability fractures, Figure 4.4(c) shows the elliptical flow geometry around the fracture tips after 5 years (just before fracture interference), Figure 4.4(d) clearly shows that the lower pressures in the stimulated reservoir volume are interfering, and Figure 4.4(e) shows that the reservoir boundaries have been felt after an unrealistically long period of time, that is, 3,000 years.

Figure 4.5 on the other hand shows similar results for the equivalent single-fracture representation of a multiply-fractured system. Figures 4.5(a) through (c) show linear flow into the high-permeability fractures, Figure 4.4(c) shows elliptical flow, while Figure 4.4(e) clearly shows boundary-dominated flow. We observe that the fracture interference, which was observed in the multiple-fracture case is absent in the single-fracture representation because it has a single fracture.

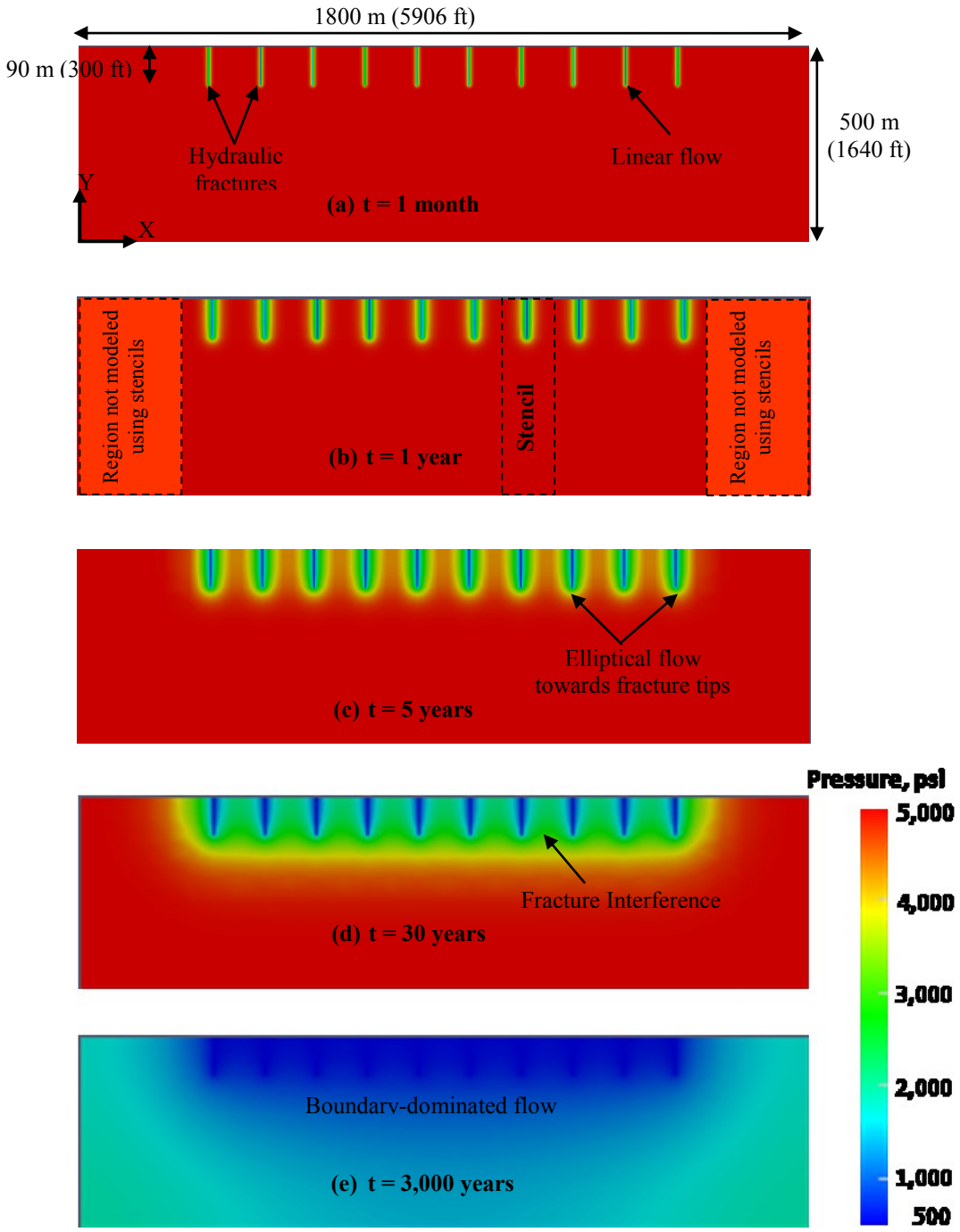

Figure 4.4—Plan view of pressure profiles shows linear flow, elliptical flow to fracture tip, fracture interaction and boundary-dominated flow for a multiple-fracture system.

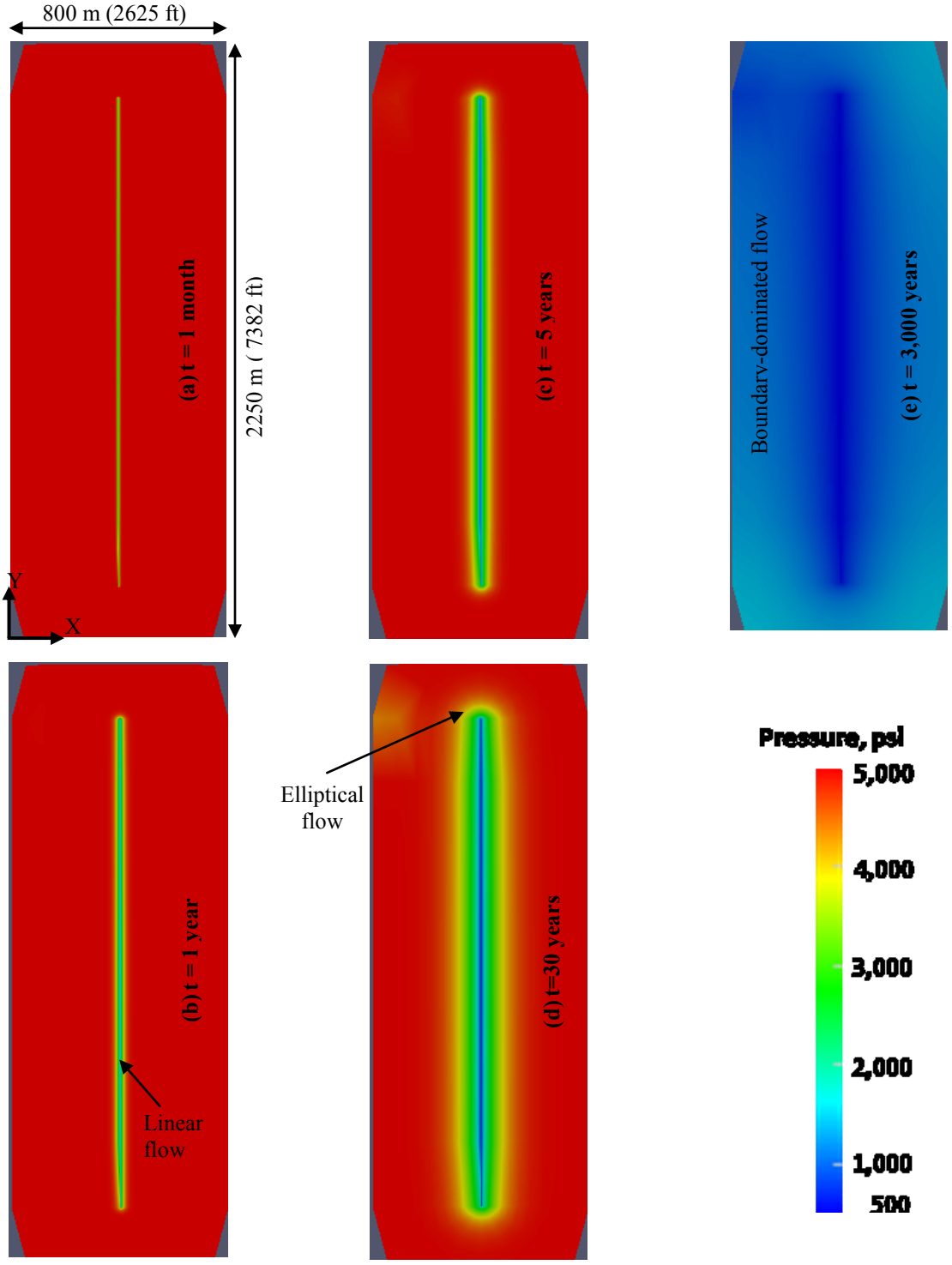

Figure 4.5—Plan view of pressure profiles shows linear, elliptical and boundary-dominated flow for a single-fracture system.

4.2 Evaluation of the Use of a Stencil to Reduce Problem Size

The objective of this study is to assess the accuracy of representing a multiply-fractured well system by a stencil. This concept was introduced by Freeman et al. (2010), and the description of the grid is provided in Section 3.2.2. The use of a repetitive element can significantly reduce the size of the grid, and consequently, the order of the Jacobian matrix and the corresponding computational requirement. The memory and execution time savings are obvious in realistic fractured shale-gas systems that can have as many as 60 hydraulic fractures (Jayakumar, Sahai and Boulis, 2011).

When using the stencil to obtain the rate forecasts for the full system, we simply multiply the rates for the minimum repetitive element by the number of times the stencil appears in the reservoir. Figure 4.6 gives the comparison of the rates for the multiply-fractured system to the rate forecast for the stencil. The results of the two cases are practically identical until after about 30 years, when the linear-flow regime ends and we begin to see fracture interference in the multiple-fracture case.

The deviation of the stencil solution from the full-scale solution after 30 years can be attributed to the differences in the contributions from boundary-dominated flow. We observe that the full-scale solution, which has a larger unstimulated matrix volume, exhibits slightly higher rates than the stencil model during boundary-dominated flow because the unstimulated volume to the left and right of the full reservoir domain, which is clearly shown in Figure 4.4(b), is not captured using the stencil. In conclusion, we can say that the use of the stencils provides near-perfect approximation within the normal reservoir economic life (usually, less than 30 years).

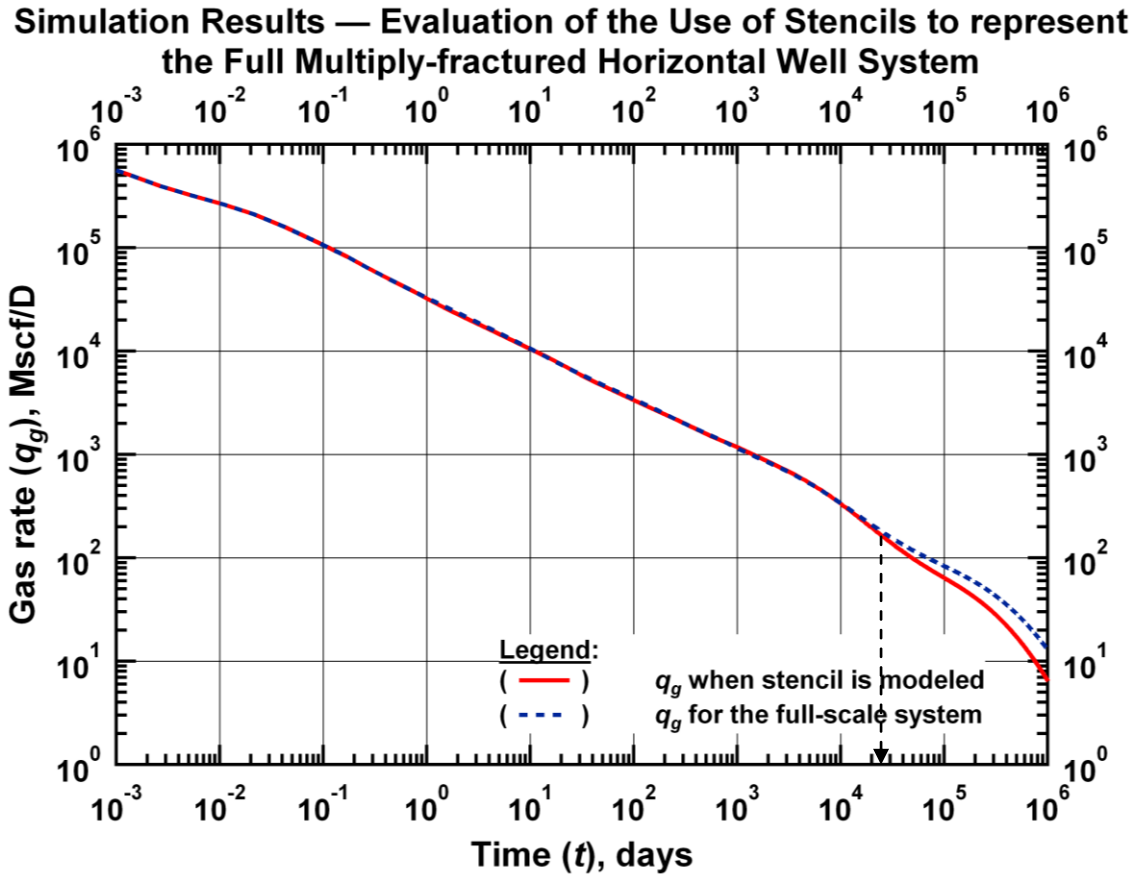

Figure 4.6—Rate profiles show that the representation of the full reservoir domain by a stencil provides a good approximation until very late in the reservoir life (over 50 years).

4.3 Distinguishing Between the Effects of Fracture Permeability and Fracture Aperture

Table 4.1 gives four different combinations of fracture permeability and aperture that yield the same fracture conductivity of 492 md-ft (1.5×10^{-10} mm-m^2). The fourth case has a fracture aperture which is larger that we can expect in reality, but it has been included in this study to highlight the trend of the production rates as the fracture aperture increases

Table 4.1—Variation of fracture permeability and aperture

Case #	w_f, mm	w_f, ft	k_{frac}, m^2	k_{frac}, md	$\phi_{modified}$
1	3	0.010	$5.0x10^{-11}$	50,000	0.33
2	15	0.049	$1.0x10^{-11}$	10,000	0.066
3	30	0.098	$5.0x10^{-12}$	5,000	0.033
4	100	0.328	$1.5x10^{-12}$	1,500	0.0099

The last column in the table shows the values of the modified porosity, which is introduced in order to keep the mass of fluid in the fractures the same in all cases, despite the increase in fracture aperture. A review of the underlying material balance equation shows that although the flows from the fractures into the well are the same in all cases, the volume of the grid cells corresponding to the fractures increase as the fracture aperture increases. This results in a consequent increase in the mass of gas in these fracture cells, and explains why higher rates are observed at very early times (corresponding to a t_D value less than $4x10^{-5}$ or less than 1 day of production for the system under study) in Figure 4.7.

The figure also shows that the representation of hydraulic fractures (which have fracture apertures in the range of a thousand or few hundreds of microns) with wider fracture apertures only impacts the very-early time behavior of the fractured system, and may not have any influence on the long-term estimates of reservoir performance.

First, we define a porosity-modification factor, f_ϕ, as the ratio of the reference fracture aperture (w_{ref}) to the current fracture aperture (w_{new}), i.e. mathematically,

$$f_\phi = w_{ref} / w_{new} \quad \text{..... 4.1}$$

The modified porosity ($\phi_{modified}$) is given as:

$$\phi_{\text{modified}} = \phi \times f_\phi \quad \text{..... 4.2}$$

where ϕ is the original or actual porosity in the reference case (that is, case #1 in Table 4.1).

In simple terms, this approach requires that if the fracture aperture is doubled, then the fracture porosity needs to be halved to maintain the same fluid mass in the grid-blocks representing the fracture.

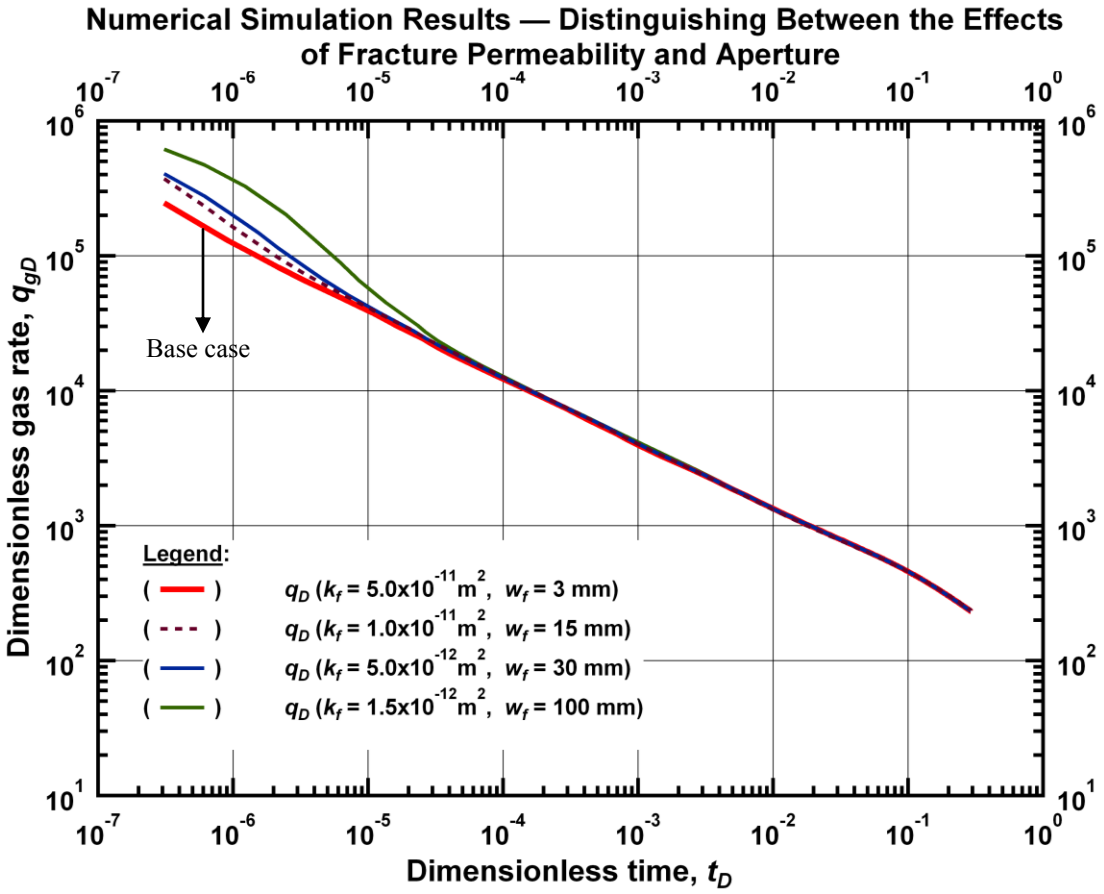

Figure 4.7—Comparison of different fracture permeability and aperture combinations that yield the same conductivity.

When the fluid mass in the fracture cells is kept constant by using the modified porosity values, the production signatures (*i.e.*, the q_D versus t_D curves shown in Figure 4.8) coincide, implying that it is not possible to distinguish between the separate effects of fracture permeability and fracture aperture. Hence, fracture-conductivity, which is the product of these two quantities, should be treated as a single entity when history-matching.

Since the production rates in Figure 4.8 are identical despite the increasing fracture aperture (provided the fracture conductivity is kept constant), there is a possibility of representing a very minute fracture aperture with a bigger one in order to reduce the number of grid-blocks required for a simulation. The reduction in the problem size is because the range of values that the size of the grid-blocks straddles in the logarithmic spacing (discussed in Section 3.1.1) is now much narrower, and this translates into the use of fewer grid cells. Although, the use of stencils, as discussed in Section 4.2, is likely to yield even fewer grid-blocks, it is important to note that for complicated fractured systems in which each fracture has a different

orientation, geometry and dimension, the minimum representative element will be much bigger in size than as shown in Figure 3.4.

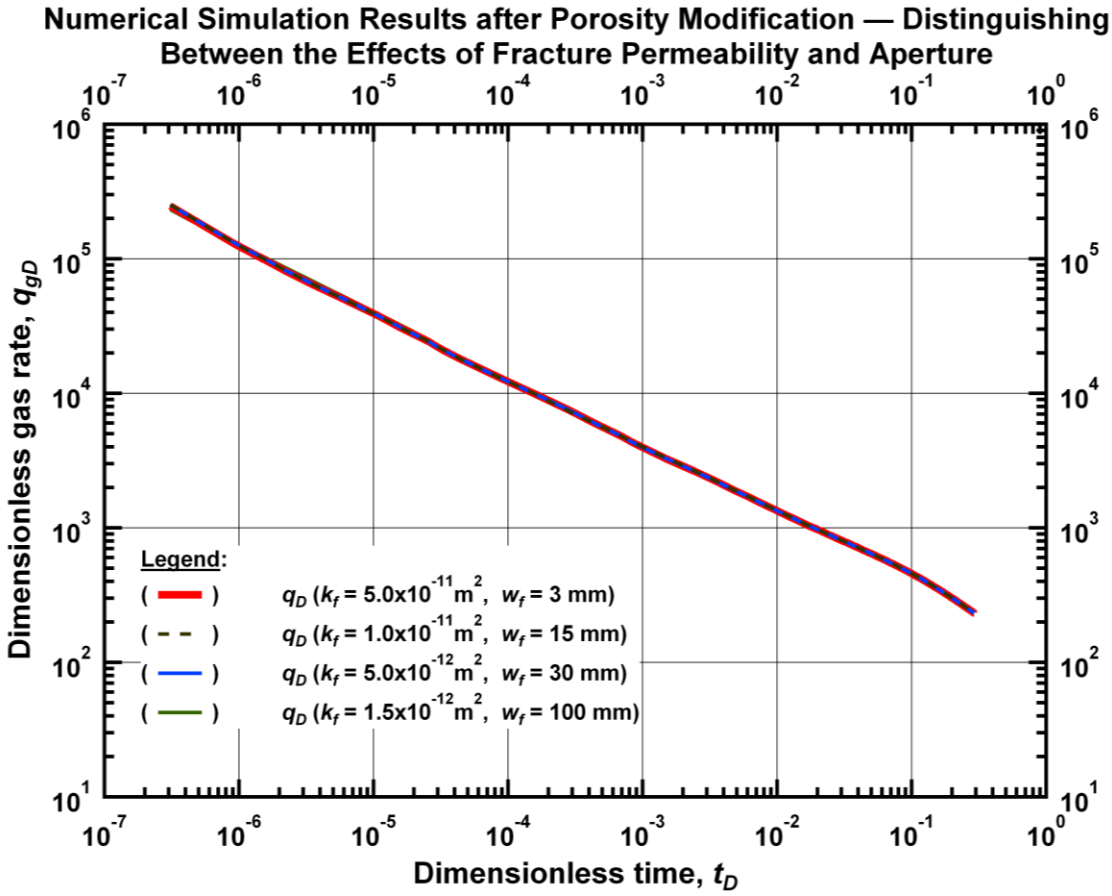

Figure 4.8—Comparison of different combinations of fracture permeability and fracture aperture, with porosity modification.

4.4 Analysis of Production from Non-planar and Non-orthogonal Fractures

Schematics and descriptions of the grids for the non-planar and non-orthogonal fractures studied in this section can be found in Sections 3.2.3 and 3.2.4 respectively. We model a non-planar fracture system (with each fracture at an angle of 60° to the horizontal) and two non-orthogonal systems (with $\theta = 60^o$ and 30^o, respectively). In all three cases, the fracture half-length, x_f is set equal to 104 m (341 ft), and this corresponds to the total fracture half-length, l_t, introduced in Figure 4.9.

In addition to the non-planar and non-orthogonal fracture systems, we model three planar orthogonal fracture systems that have their fracture half-lengths set equal to l_t, l_{a60} and l_{a30} respectively, as illustrated in Figure 4.9.

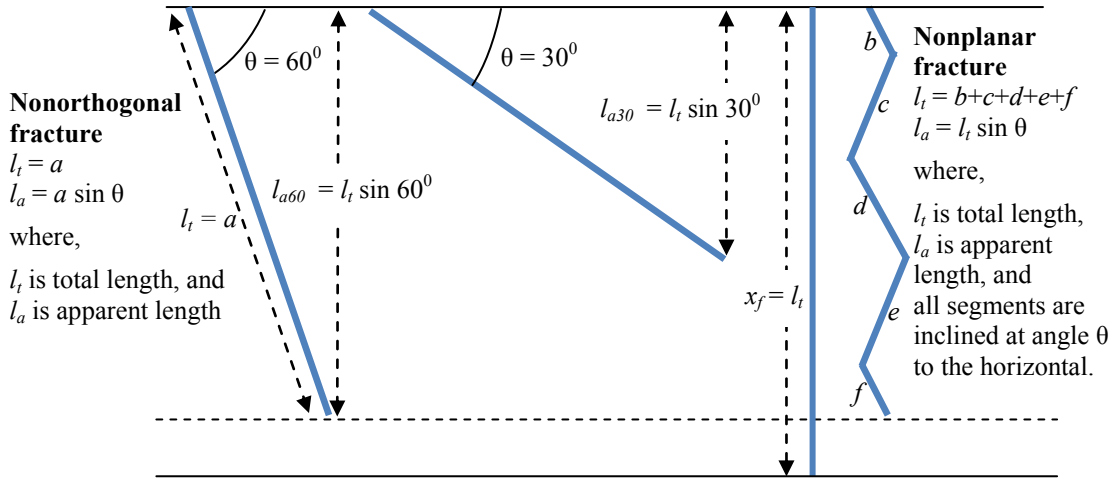

Figure 4.9—Schematic diagram illustrating the concept of apparent and total lengths for non-planar and non-orthogonal fractures.

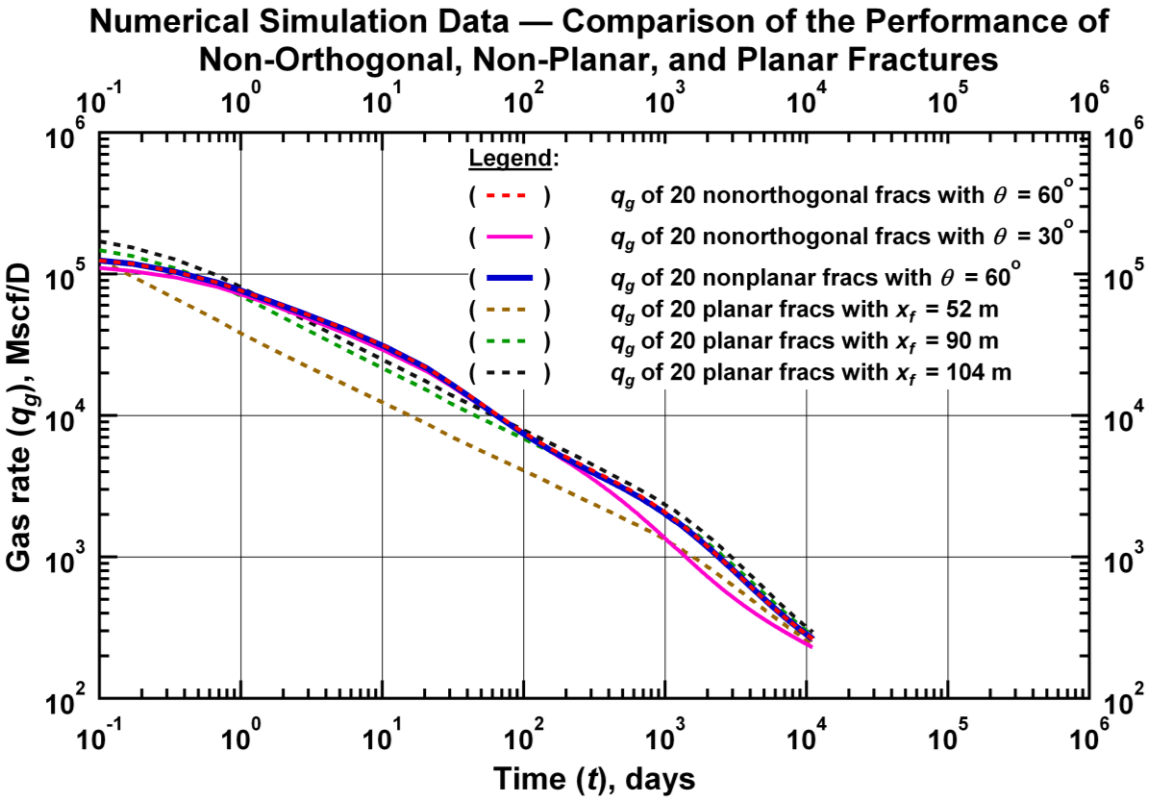

Figure 4.10—The flow profile for non-planar and non-orthogonal fractures with $\theta = 60^o$ look identical. The non-orthogonal case with $\theta = 30^o$ exihibits fracture interference earlier than the other cases because it has a much lower apparent fracture half-length, l_a.

Figure 4.10 shows an almost identical rate profile for the non-planar and non-orthogonal fracture systems at an angle of 60^o to the horizontal. The fracture interference in these two cases becomes evident at the same time with the planar case that has a fracture half-length equal to the apparent length, l_a. We also observe that the non-orthogonal fracture case with $\theta = 30^o$ exhibits fracture interference earlier than the other cases, and this can be attributed to the fact that the apparent fracture half-length, l_a, as well as the apparent area of the SRV (illustrated in Figure 3.8(a)) is smaller in comparison to the other non-ideal cases.

The cumulative production plot in Figure 4.11 shows that the non-ideal fractured systems have lower production than the planar cases with the same fracture half-length. This implies that to the extent possible, fractures should be designed such that their angle of inclination with the horizontal well should be as close to 90^o as possible. This can arguably be achieved by ensuring that the horizontal well is drilled in the direction of the minimum principal stress, as fractures usually propagate perpendicularly to the direction of the minimum principal stress.

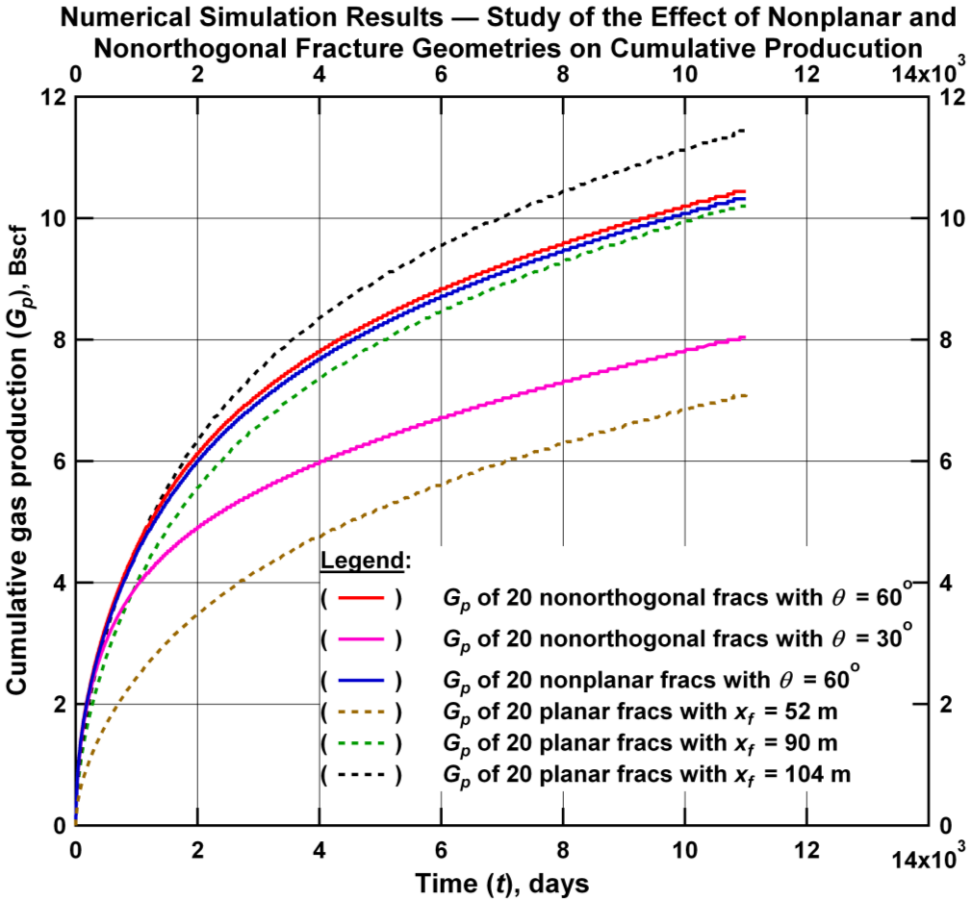

Figure 4.11—Cumulative production profile initially matches that of a planar fracture with a total half-length, but the production gradually drops due to smaller apparent area of SRV when fracture interference begins.

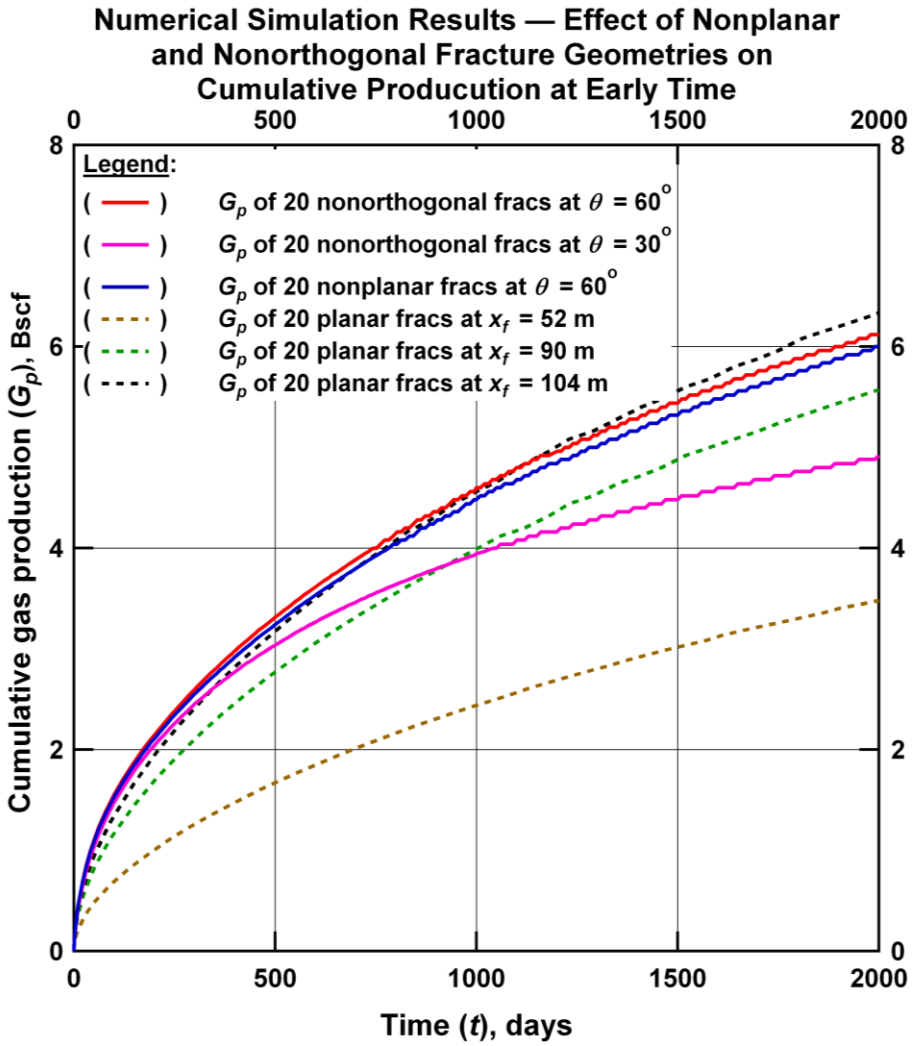

Figure 4.12—Early-time cumulative production plots show that all cases with x_f = 104 m (341ft) have almost identical production in the linear flow period.

Figure 4.12 presents the same data in Figure 4.11, but we have reduced the range of time shown so that we can see the relative behavior of the non-ideal fracture cases more clearly. We observe that the production profiles for all cases with a fracture half-length of 104 m (341 ft) are very similar, but the production of the non-orthogonal and non-planar fractures later drop below the planar equivalent case with the same fracture half-length. As expected, the non-orthogonal case at an angle of 30° is the first to exhibit the reduced production, and this could be attributed to the reduced apparent SRV, because it has the smallest apparent length, l_a.

The three dotted lines in the cumulative production plots of Figure 4.12 correspond to the three planar cases illustrated in Figure 4.9. We observe from Figure 4.11 that the planar cases with $x_f = l_a$ have lower

rates than the corresponding non-orthogonal cases because the surface areas of the fracture face ($x_f * h$) are smaller in these equivalent planar cases.

The square-root plots for the three non-ideal and the three planar fracture systems are given in Figure 4.13. The slopes for all the non-ideal cases (the continuous lines) are almost identical with that of the planar case (with x_f = 104 m) during linear flow because they all have the same fracture surface area, and these slopes are generally indicative of the area of the SRV when the reservoir exhibits linear flow, as discussed in Section 4.1. The steeper slope of the planar fracture case with x_f = 52 m in the labelled linear flow period is also expected because the area of the SRV is inversely proportional to the slope of the square-root plot, and this implies that the area of the SRV is smaller in this case. Finally, we observe from the square-root plot (as well as the log-log plot discussed previously) that the earliest deviation from linear flow is in the non-orthogonal fracture system, which is at an angle of 30° to the horizontal.

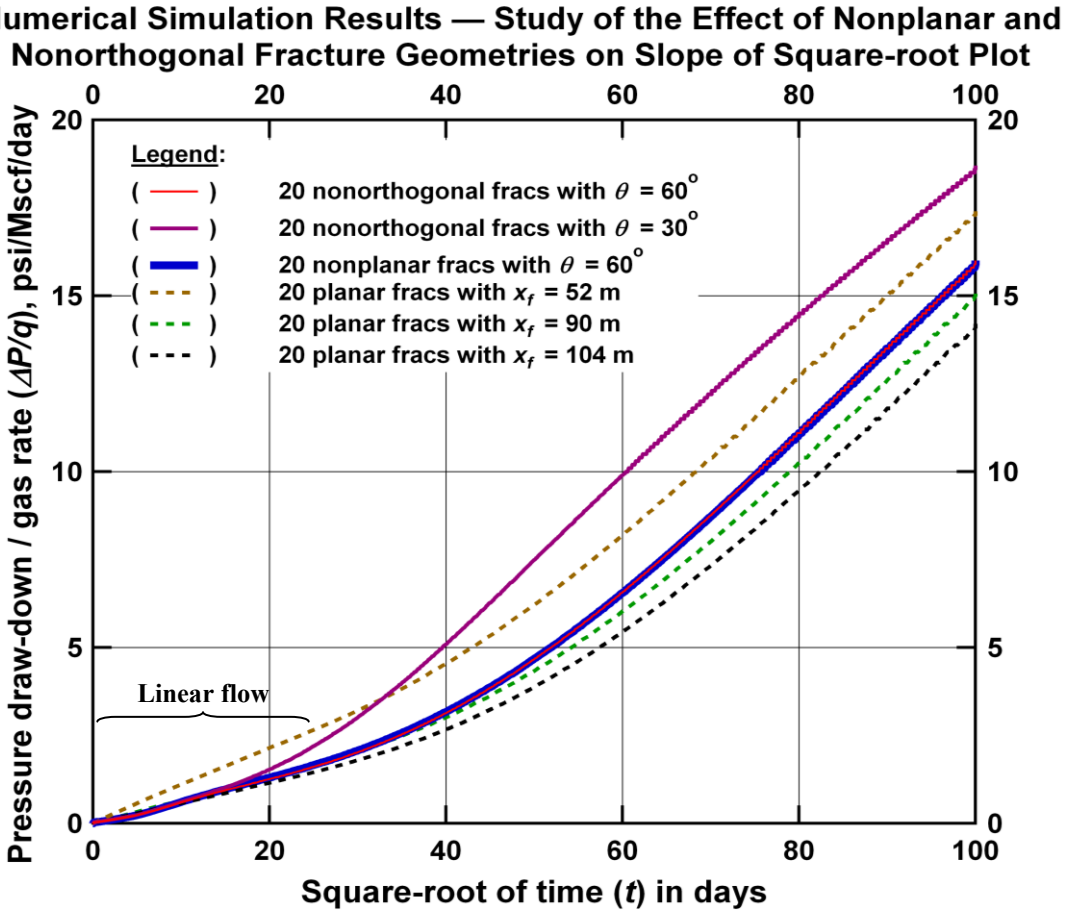

Figure 4.13—Square-root plot shows an almost identical slope for the non-ideal cases when the square-root time is less than 20. This is in agreement with the fact that all three non-ideal cases have the same fractue half-length, and hence same area ($x_f * h$).

Figure 4.14 presents a plan view of the pressure profile for a non-planar fracture system at different times. Figure 4.14(a) shows linear flow in a direction that is orthogonal to the fracture face, which is non-planar. From figure 4.14b we observe that there is some pressure interaction at the sharp corners of the non-planar fracture, and this results in an apparent decrease in the fracture half-length of these fractures; hence, the reduced producton observed in Figure 4.12 (after about 650 days). After 5 years of production history, we observe (from Figure 4.14(c)) that there is fracture interference, and the width of the SRV is 90 m. Figure 4.14(d) shows the slow progression of the pressure profile into the low-permeability matrix.

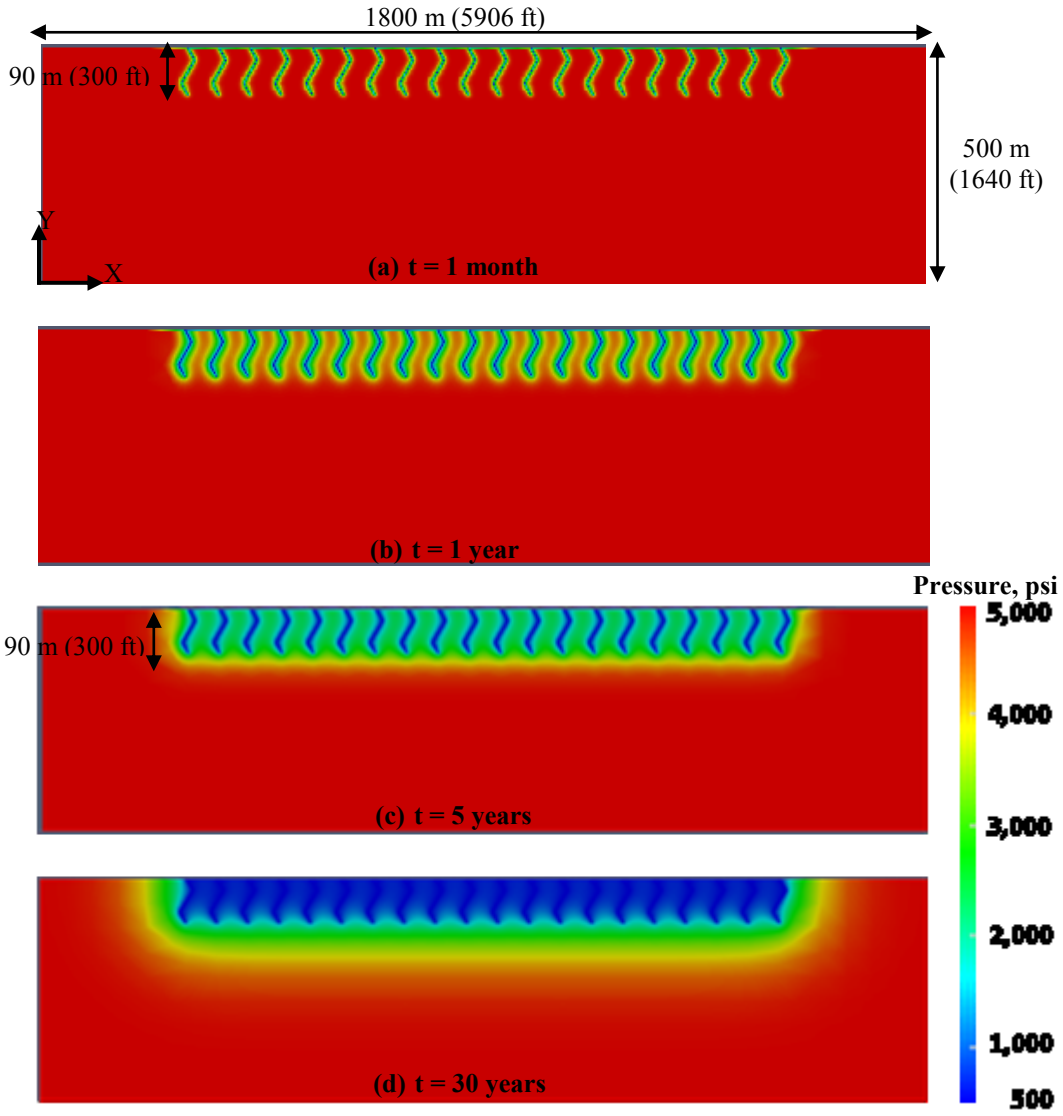

Figure 4.14—Plan view of pressure profiles at (a) 1 month, (b) 1 year, (c) 5 years, and (d) 30 years shows linear flow, pressure interference at fracture corners, fracture interence and SRV flow, respectively.

Figure 4.15 shows how the pressure profile of a non-orthogonal fracture (with an inclination angle of 60°) evolves through time. Figures 4.15(a) and (b) shows linear flow, while Figure 4.15(c) shows fracture interference, with a SRV width of 90 m. The identical value of SRV width in Figures 4.14(c) and 4.15(c) explains why the rate profiles, cumulative production and square-root plot of the two cases are practically identical, as seen in Figures 4.10 – 4.13. Figure 4.15 shows the slow drainage of the unstimulated reservoir volume after 30 years.

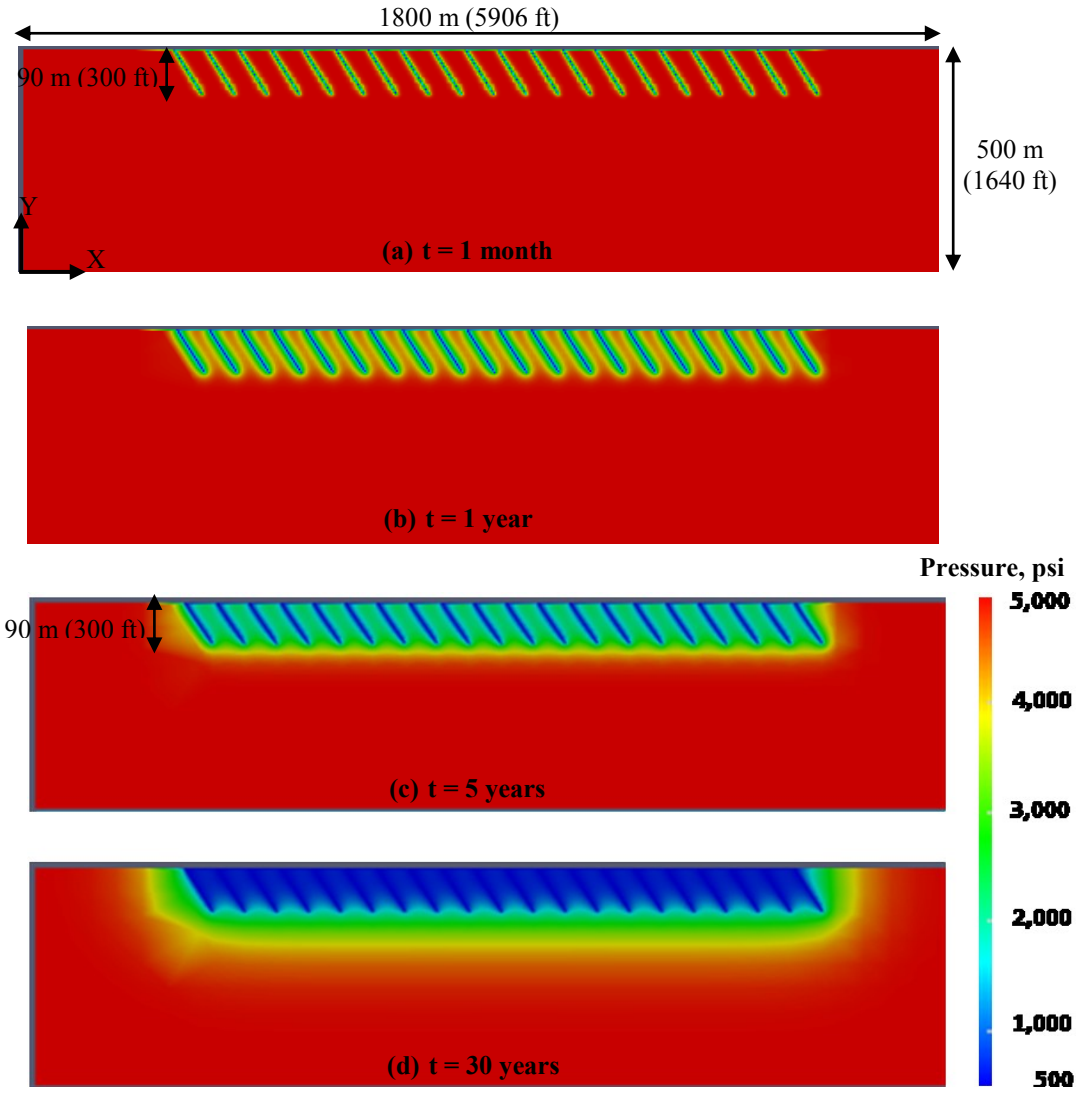

Figure 4.15—Plan view of pressure profiles at (a) 1 month, (b) 1 year, (c) 5 years, and (d) 30 years shows the evolution of pressure with time in a non-orthogonal fracture system with $\theta = 60^{o}$.

Figure 4.16 is very similar to Figure 4.15, except that in this case, the inclination angle is 30° to the horizontal well. This difference in inclination angle causes a reduction in the apparent fracture half-length to a value of 52 m (170 ft), in comparison to the previous case, where the apparent fracture half-length is 90 m (300 ft), as illustrated in Figure 4.9. The significant reduction in production as the fracture angularity is reduced from 60° to 30° (seen in Figures 4.10 – 4.12) may be attributed to the reduction in the SRV width from a value of about 90 m to about 52 m (as shown in Figures 4.15(c) and 4.16(c), respectively).

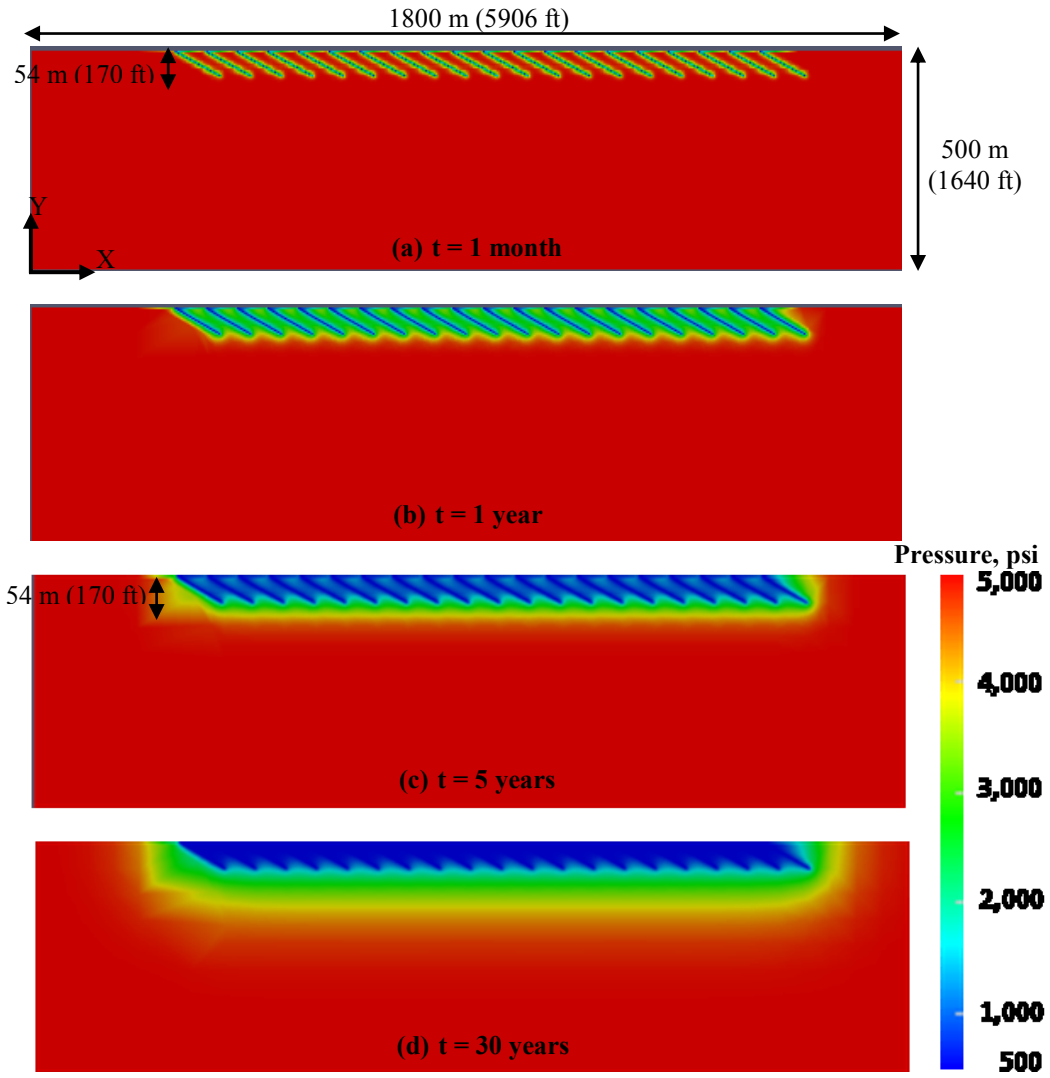

Figure 4.16—Plan view of pressure profiles at (a) 1 month, (b) 1 year, (c) 5 years, and (d) 30 years shows the evolution of pressure with time in a non-orthogonal fracture system with $\theta = 30^{o}$.

4.5 Analysis of Production from Secondary Fractures

Houze et al., (2010) pointed out that it is unlikely that a coupled primary-secondary fracture network behaves like a single "effective primary fracture system", and that such coupled fractured systems can only be evaluated using a mesh-maker with a gridding scheme for the secondary fracture networks. TAMMESH provides this functionality, and a detailed description of the three different configurations of the induced fractures modeled in this research is given in Section 3.2.5. Additionally, we have modeled a case in which the coupled primary-secondary fracture system is represented with an effective primary fracture system. This was achieved by using more primary fractures, such that the total sum of the surface areas of all the fractures in the effective primary fracture system is the same as the sum of the surface areas of the secondary and primary fractures in the coupled primary-secondary fracture system.

We have also modeled a system with only primary fractures (hence, smaller SRV) which serves as the reference case used for the comparison. Table 4.2 shows the values of the secondary fracture parameters, in addition to a list of the corresponding values of the equivalent or proxy model, which uses fewer and wider grid blocks with a porosity modification as illustrated in Section 4.2. The conductivity of the secondary fracture in both the actual and proxy model is 16.4042 md-ft (5×10^{-12} mm-m^2).

Figure 4.17 gives the log-log rate profile for all the five cases. From this figure we observe that:

- The production rates for the secondary fracture at $h/4$ from the reservoir top is practically identical to that for the centered secondary fracture because the SRV is the same in both cases. The slight difference in production rates during fracture drainage (which does not last up to a day) is because the fractures drain directly into the wells in the centered secondary fracture case.
- The existence of secondary fractures significantly enhances production. Figure 4.17 shows that this increase in production is strongly dependent on the surface area of the induced fractures.
- The case with two secondary fractures (at $h/4$ and $3h/4$ from the reservoir top) has the highest rate of production. This is expected because this case corresponds to the largest SRV.
- The primary-fracture representation of a coupled primary-secondary fracture system (delineated by the brown dotted line), closely matches the secondary fracture cases that have the same SRV, especially in the linear flow regime. Hence, the representation of such coupled primary-secondary fracture systems with an effective primary-fracture system may be a good approximation.

Table 4.2—Secondary fracture parameters

	ϕ	w_f, mm	w_f, ft	k_{frac}, m^2	k_{frac}, md
Actual	0.9	0.05	0.00016	1.0×10^{-10}	100,000
Proxy	0.0005	100	0.32808	5.0×10^{-14}	50

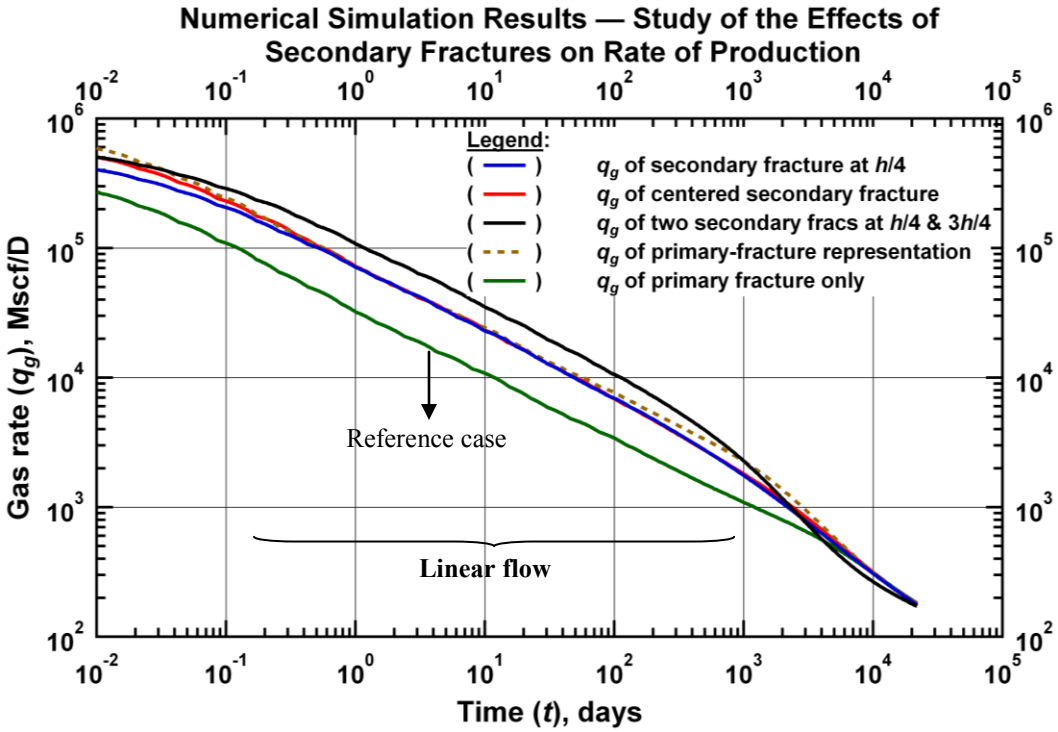

Figure 4.17— Log-log rate profile highlights trends in secondary/primary fracture interaction.

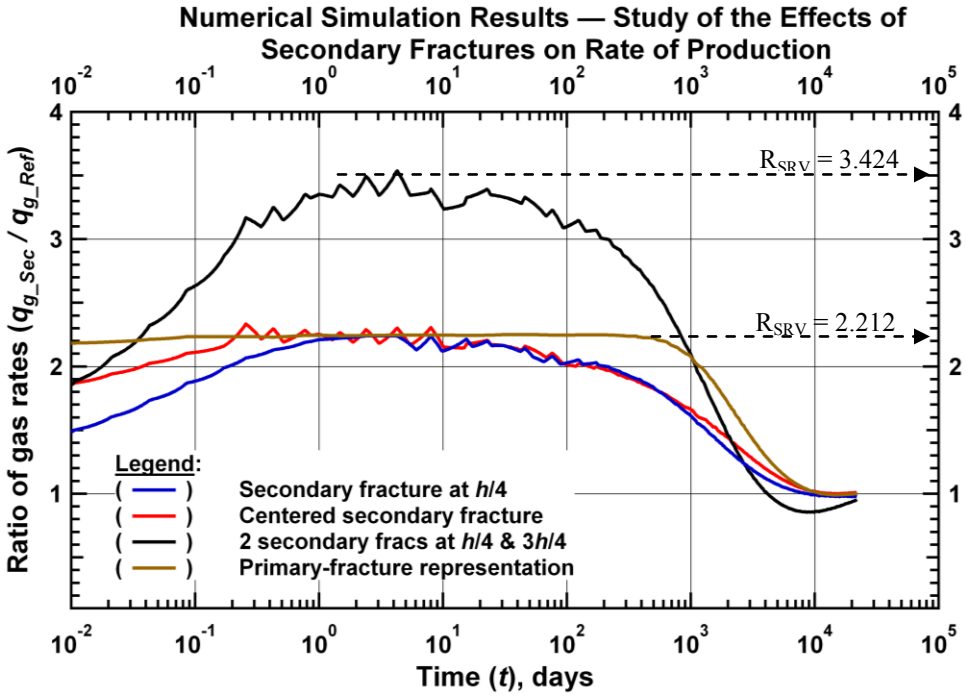

Figure 4.18—Ratio of the flow rates of the coupled primary-secondary fracture cases to the reference primary fracture case peaks at a value that is equal to the ratio of fracture surface areas.

The ratios of the flow rates of the secondary fracture cases to the reference primary fracture case (shown in Figure 4.18) peaks at a value which is approximately equal to the ratio of the sum of the fracture surface areas of the secondary fracture systems to the sum of the fracture surface area of the reference primary fracture system. This ratio is called the SRV ratio and is mathematically defined as:

$$R_{SRV} = A_{SF} / A_{ref}$$

where, A_{SF} is the SRV area of the coupled primary-secondary fracture system and A_{ref} (m^2 or ft^2) is the area of the SRV for a reference case, which is a primary fracture system with no secondary fractures. In all cases, the breadth of the secondary fracture's surface area is two times the primary fracture half-length, while its length is equal to the total length of the horizontal well, as shown in Section 3.2.5. Hence, the dimension of the surface of a single secondary fracture is 4000 ft X 600 ft (1200 m X 90 m).

The modeling of secondary fractures as continuous horizontal high-permeability streaks could be a good approximation since the SRV has been shown (in the results of Section 4.4 and in Figures 4.17 and 4.18) to have the most significant effect on production. Therefore, the less consequential effects of angularity and discontinuity in fracture geometry are neglected in the modeling of these secondary fractures.

To obtain the R_{SRV} ratio for a coupled primary-secondary fracture with a single secondary fracture, we add the area of the secondary fracture to that of the primary fracture (10*600 ft X 330 ft or 10*180 m X 100 m, i.e., number of primary fractures * $2x_f$ * h), then divide this by the area of the reference primary fracture. Therefore,

$$R_{SRV} = \frac{(4000 \times 600 + 600 \times 330 \times 10)}{600 \times 330 \times 10} = 2.21212$$

Figure 4.19 presents the same results shown in Figure 4.17 but in terms of dimensionless rates and times. The normalization of the rates and times using the dimensionless quantities results in a match of all the five cases during linear flow. We observe that although the total life of all the fractured systems is the same, the corresponding value in dimensionless time is different. From Eq. 2.2, dimensionless time is inversely proportional to square of the total fracture half-length for a given fractured system. Hence, the values of the dimensionless times reduce as the total fracture half-lengths (and consequently the SRVs) increase during fracture interference, when the flow rates for all the five cases shown in Figure 4.17 are almost identical. Similarly, this figure shows that the extent of the deviation from the reference case (i.e., with SRV = 1) increases as the SRV ratio increases.

Although the primary-fracture representation of the secondary system shows only a slight deviation from the single secondary fracture cases (when $t_D >= 10^{-3}$), the difference is still too small to make any conclusive argument. However, it is important to note that the primary and secondary fractures were modeled using an infinite fracture conductivity value, and it might be very difficult to accurately represent

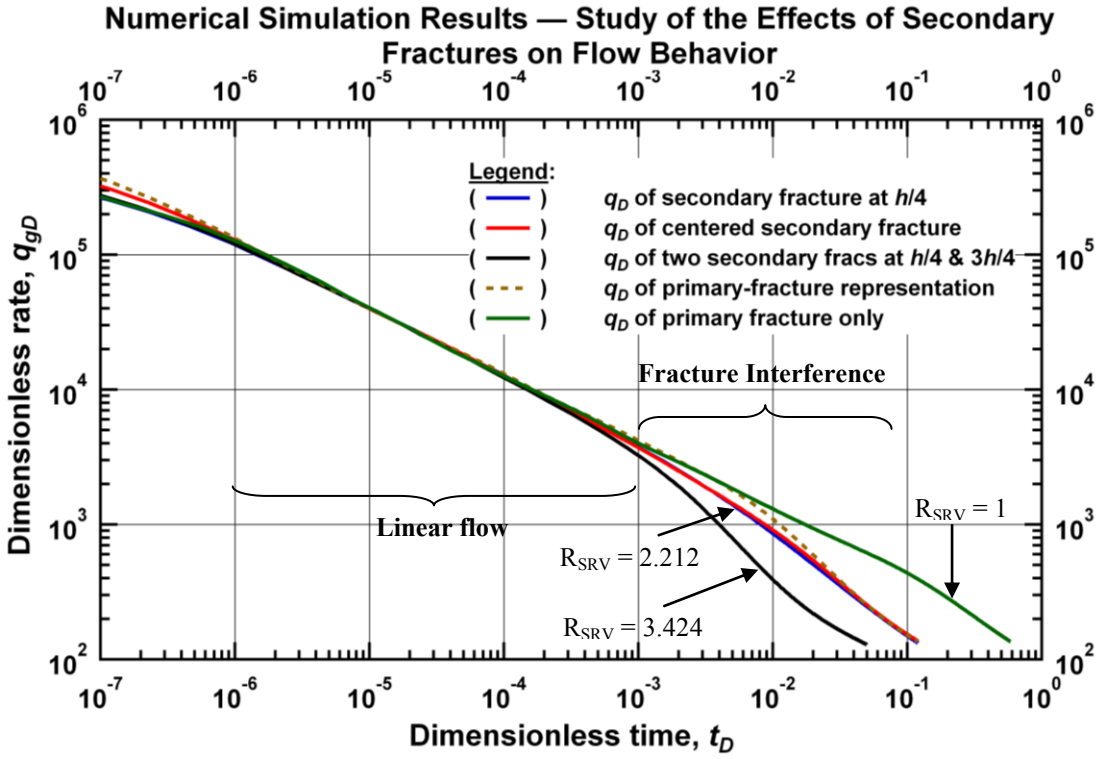

Figure 4.19—Dimensionless rate profile highlights trends in secondary/primary fracture interaction.

a coupled primary-secondary fracture system, which has a combination of infinite-conductivity primary fractures and finite-conductivity secondary fractures, with a primary-fracture system.

Figure 4.20 presents a 3D view of the pressure profile for a coupled primary-secondary fracture system with a laterally-extensive secondary fracture that intersects the primary fractures at 90^o and at a depth of h/4 from the top of the primary fracture (as illustrated in Section 3.2.6 with the schematic given in Figure 3.16). The pressure profiles show that the stimulated reservoir volume is significantly increased by the presence of the induced fractures, in addition to the primary fractures.

After the drainage of the region in between the primary fractures, the contribution of the induced fractures to production becomes less significant (as seen in Figure 4.20(d)) and this explains the drop in the production rate to approximately the same value after 30 years of production (seen in Figure 4.17). The production at this time is predominantly from the slow drainage of the low-permeability matrix, and this provides some explanation for the very low production rates after 30 years of production. Additionally, the pressure profiles in Figure 4.20(a) and (b) show that the perforated horizontal well does not contribute significantly to production due to its small surface area.

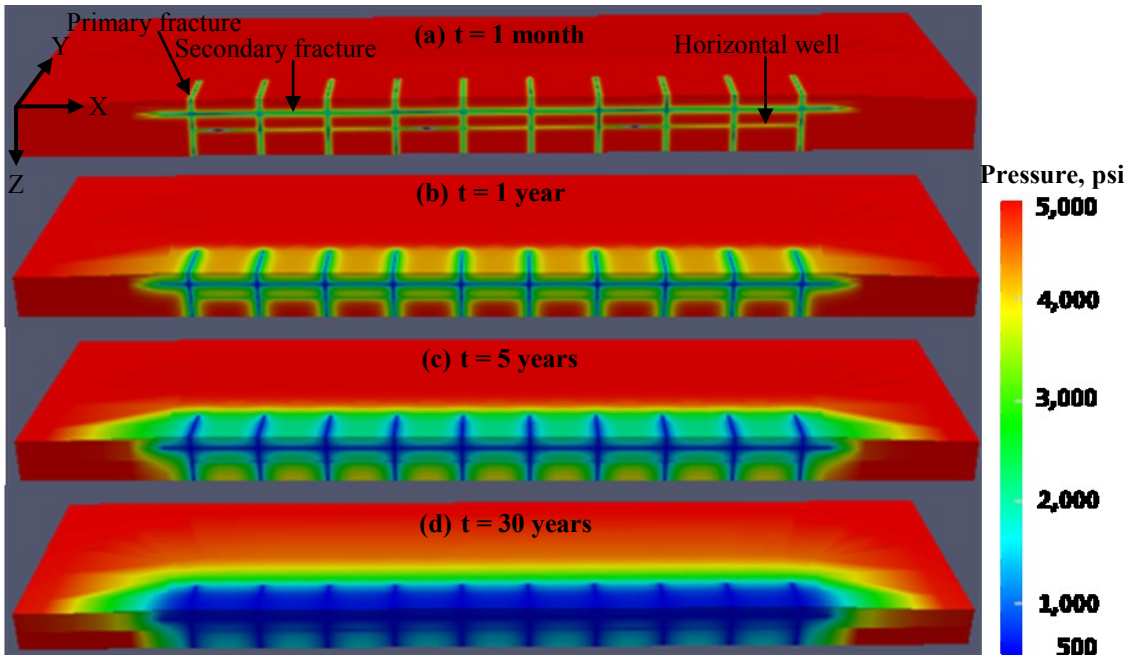

Figure 4.20—3D view of pressure profiles at (a) 1 month, (b) 1 year, (c) 5 years, and (d) 30 years shows the propagation of the pressure front in a coupled primary-secondary fracture system.

4.6 Study of the Effect of Secondary Fracture Conductivity on Production

Figure 4.21 shows the effect of the variation in the conductivity of secondary fractures on flow performance, and Table 4.3 lists the fracture properties used in all scenarios studied. The following can be observed from the simulation results given in Figure 4.21:

- For dimensionless secondary fracture conductivity values greater than 55.6 (*i.e.*, infinite-conductivity secondary fractures), production rate is unaffected by an increase in secondary fracture conductivity.
- For dimensionless secondary fracture conductivity values less than 11.1 (*i.e.*, finite-conductivity secondary fractures), production rate decreases as the dimensionless fracture conductivity decreases. This decrease in production is evidenced by the drop in value of the half-slope (representing linear flow) to a value that is less than 1/2.
- All nine curves are practically identical during fracture interference. This may be attributed to a strong influence of the stimulated reservoir volume, which is identical in all nine cases.

Table 4.3—Secondary fracture conductivity parameters

Case #	k_{frac}, md	k_{frac}, m^2	C_f, mm-m^2	C_f, md-ft	C_{fD}
1	3×10^{6}	3×10^{-9}	1.5×10^{-10}	4.92×10^{2}	1.67×10^{4}
2	2×10^{6}	2×10^{-9}	1.0×10^{-10}	3.28×10^{2}	1.11×10^{4}
3	1×10^{6}	1×10^{-9}	5.0×10^{-11}	1.64×10^{2}	5.56×10^{3}
4	2×10^{5}	2×10^{-10}	1.0×10^{-11}	3.28×10^{1}	1.11×10^{3}
5	1×10^{5}	1×10^{-10}	5.0×10^{-12}	1.64×10^{1}	5.56×10^{2}
6	1×10^{4}	1×10^{-11}	5.0×10^{-13}	1.64×10^{0}	5.56×10^{1}
7	2×10^{3}	2×10^{-12}	1.0×10^{-13}	3.28×10^{-1}	1.11×10^{1}
8	1×10^{3}	1×10^{-12}	5.0×10^{-14}	1.64×10^{-1}	5.56×10^{0}
9	2×10^{2}	2×10^{-13}	1.0×10^{-14}	3.28×10^{-2}	1.11×10^{0}

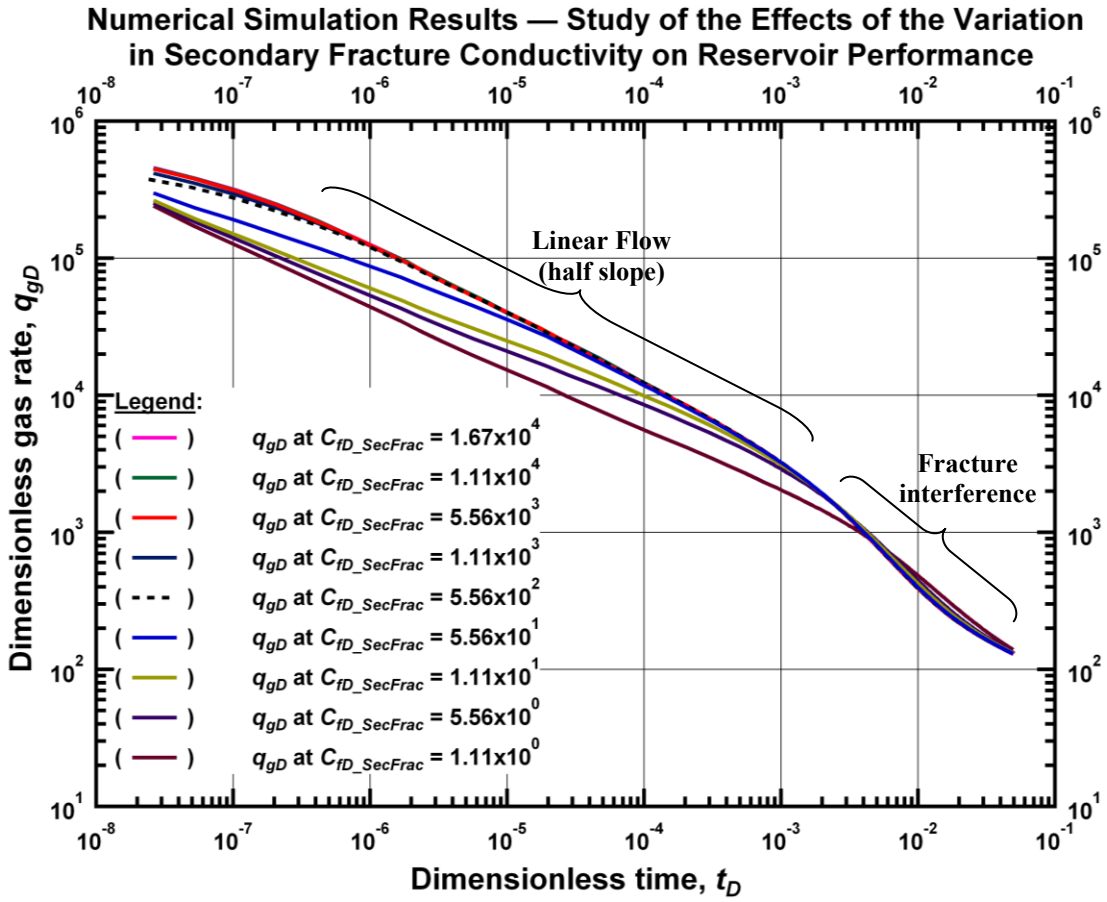

Figure 4.21—Dimensionless rate profiles show a reduction in the slope of the linear flow regime when the dimensionless conductivity of the secondary fractures becomes less than 10 (depicting finite conductivity).

Table 4.4 gives the fracture properties used in the study on the effect of variations in fracture conductivity on production, in a reservoir with only primary fractures. The simulation results shown in Figure 4.22 agree very well with earlier results of Freeman (2010). For the specific cases studied, the results suggest that the effect of primary fracture-conductivity variation on production appears to be stronger in comparison to the effect of secondary fracture-conductivity variation (given in Figure 4.21). We observe a significant reduction in production rates relative to the infinite-conductivity primary-fracture cases, when the dimensionless fracture conductivity becomes less than or equal to 11; the production rates drop even further as the dimensionless fracture conductivity decreases.

Table 4.4—Primary fracture conductivity parameters

Case #	k_{frac}, md	k_{frac}, m^2	C_f, mm-m^2	C_f, md-ft	C_{fD}
1	$5.00x10^{6}$	$5.00x10^{-9}$	$1.5x10^{-8}$	$4.92x10^{4}$	$1.67x10^{6}$
2	$5.00x10^{5}$	$5.00x10^{-10}$	$1.5x10^{-9}$	$4.92x10^{3}$	$1.67x10^{5}$
3	$5.00x10^{4}$	$5.00x10^{-11}$	$1.5x10^{-10}$	$4.92x10^{2}$	$1.67x10^{4}$
4	$5.00x10^{3}$	$5.00x10^{-12}$	$1.5x10^{-11}$	$4.92x10^{1}$	$1.67x10^{3}$
5	$5.00x10^{2}$	$5.00x10^{-13}$	$1.5x10^{-12}$	$4.92x10^{0}$	$1.67x10^{2}$
6	$1.67x10^{2}$	$1.67x10^{-13}$	$5.0x10^{-13}$	$1.64x10^{0}$	$5.56x10^{1}$
7	$3.33x10^{1}$	$3.33x10^{-14}$	$1.0x10^{-13}$	$3.28x10^{-1}$	$1.11x10^{1}$
8	$1.67x10^{1}$	$1.67x10^{-14}$	$5.0x10^{-14}$	$1.64x10^{-1}$	$5.56x10^{0}$
9	$3.33x10^{0}$	$3.33x10^{-15}$	$1.0x10^{-14}$	$3.28x10^{-2}$	$1.11x10^{0}$

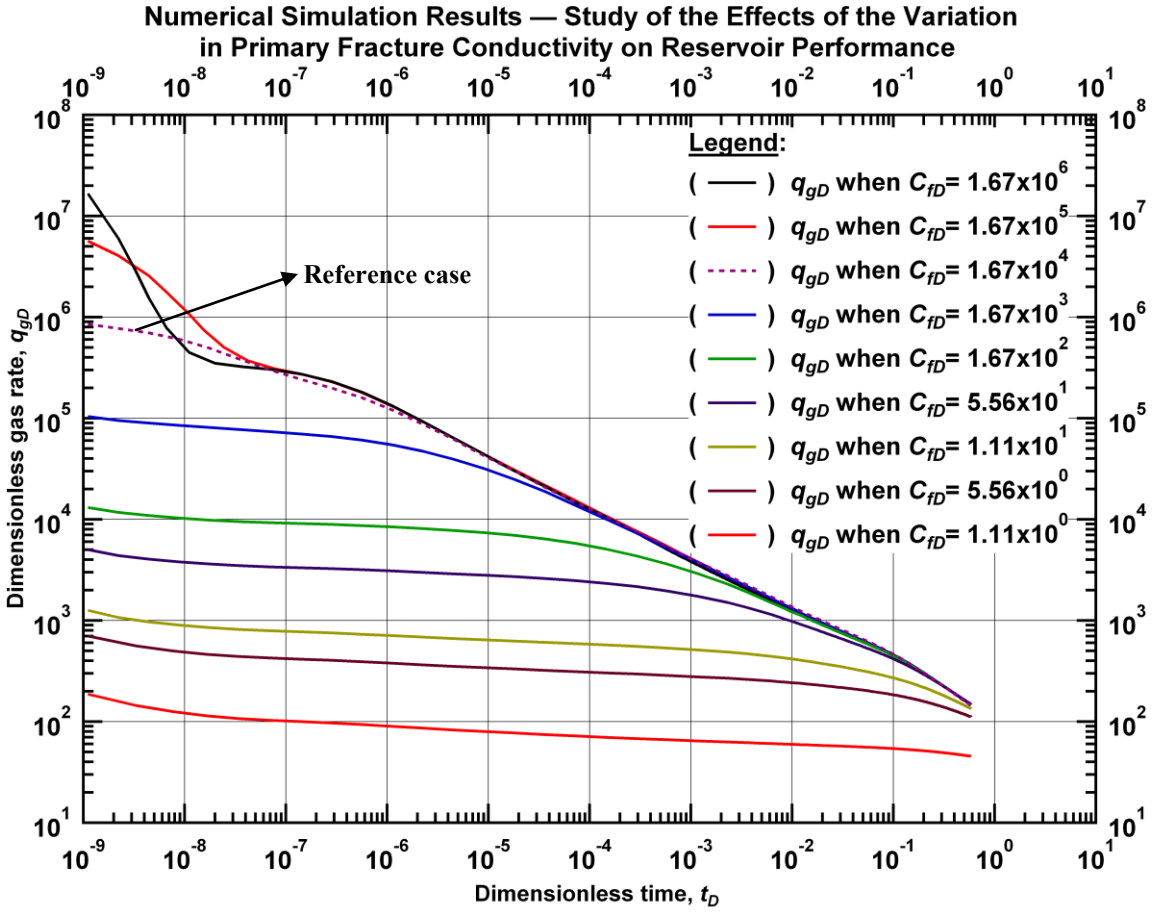

Figure 4.22—Dimensionless rate profiles show a drop in production as primary fracture conductivity drops.

4.7 Conclusions

This chapter shows that the representation of multiply-fractured horizontal well systems with either an equivalent single-fracture or with a stencil can give a good approximation to flow within normal well production life of about 30 years. The results show that the single-fracture representation overestimates the production rates during fracture interference, because this flow period does not exist for a system with a single fracture.

The stencil representation gives a more accurate representation than the single fracture representation, and it involves the use of much fewer grid-blocks because only a small fraction of the total reservoir is modeled. This can be very useful in horizontal shale-gas wells that can have up to 60 hydraulic fracture clusters. The deviation from the reference solution for a stencil representation does not appear until the onset of boundary-dominated flow (after over 55 years), and this deviation can be attributed to the

unstimulated reservoir volume on both ends of the horizontal well length, which is not modeled when using stencils.

Furthermore, the simulation results in this chapter shows that fracture conductivity should be treated as a single entity when history-matching since the effects of fracture permeability and fracture aperture appear inseparable. The study of non-ideal fracture geometries shows that these non-planar and non-orthogonal fractures, which can be expected in real-life, give progressively lower production as the angle of inclination between the fractures and the horizontal wells drops below 90^{o}, given the same hydraulic fracture half-length. This implies that when designing fracture completions, we should endeavor to keep the fractures as orthogonal to the horizontal well as possible, and this may be achieved by drilling the horizontal well in the direction of minimum principal stress.

The flow profiles for the different secondary fracture configurations show that the production rates increase as the SRVs increase, particularly during the linear flow period. Furthermore, the ratio of the flow rates of these coupled primary-secondary fracture systems peaks at a value which is approximately equal to the ratio of its SRV to that of a reference primary fracture system that has no induced fractures. The representation of an infinite conductivity secondary fracture system with an effective primary-like system shows only minor deviations from the base case, but more deviation is expected as the conductivity of the secondary fractures are reduced, and the question of what permeability to use in the primary-fracture representation becomes even more difficult to answer.

CHAPTER V
SUMMARY AND CONCLUSIONS

The goal in this research is to expand the current understanding of flow behavior in fractured tight-gas and shale-gas systems with induced fractures and non-ideal fracture geometries. To provide the flexibility required to accurately represent these complex systems, an unstructured mesh-maker called TAMMESH was constructed. This mesh-maker provides all of the required pre-processing, while the actual simulations are performed using TAMSIM, an unconventional-gas reservoir simulator developed at Texas A&M University.

In this research, cases of up to a half-million grid-blocks were constructed used to perform simulation cases of durations up to 3,000 years. The idea is to provide high-resolution reference numerical solutions that show virtually all the trends that can be expected in these unconventional gas reservoirs. The cases studied in this work provide some insight on the effect of fracture angularity, irregularities in fracture orientation, and coupled primary-secondary fracture networks on reservoir performance. The study of the effects of these irregularities in the fracture geometry on production is limited in the literature because of the difficulty in efficiently gridding such non-ideal and complex fracture systems.

Chapter I illustrates the objectives and importance of this research. A validation of the numerical simulator used in this work is provided, by comparing the simulation results with that from Ecrin, a commercial software package (Ecrin 2009). To make the results of this research easily reproducible, a table of all the reservoir and completion parameters used throughout this work is given.

Chapter II gives an overview of relevant information in the literature that forms the theoretical base for this research. I provide schematic diagrams that illustrate different fracture classifications and geometries. A detailed discussion of the numerical simulator used in this work was presented by Freeman (2010), while Rycroft (2007) provided a rigorous description of the implementation of the Voronoi library used in TAMMESH.

Chapter III details of the most important segments of TAMMESH, the unstructured mesh-maker developed as part of this project. I present several perspectives of the grids which are generated using this mesh-maker and visualized using "gnuplot", a free Unix visualization tool. In the secondary fracture cases, where the location of the induced fractures cannot be seen clearly due to the large number of grids, we provide 3D schematic diagrams that illustrate the different secondary fracture configurations. We also present a discussion of how cell centers can be placed in a pattern that yields the desired non-ideal fracture geometries when the Voronoi tessellation routine of the voro++ library is called.

In Chapter IV, all the simulation results are discussed using appropriate diagnostic plots. To confirm the flow-regime analyses, high-resolution pressure maps are provided where necessary. These analyses show

that the use of a single-vertical fracture or a stencil to represent multiply-fractured horizontal well systems yields good results during linear flow. The results become less accurate when the fractures begin to interact, since fracture interference is completely absent in a single fracture system.

The use of a "minimum representative element" called the "stencil" appears to be a very accurate and efficient approximation of the full problem because the solution for the stencil very closely matches the reference case within the normal expected production life of a well. The slight deviation observed after about 55 years (for the case studied in this research) can be attributed to the infinite-acting nature of the unstimulated region to the left and right of the first and last fractures, respectively. I also show that it may not be possible to distinguish between the effects of fracture permeability and fracture aperture on production; hence, fracture conductivity should be treated as a single entity when history-matching.

The study of non-planar and non-orthogonal fractures shows that for a given hydraulic fracture half-length, production reduces as the angle of inclination drops below 90^{o}. This implies that when designing fracture completions, we should endeavor to keep the fractures as orthogonal to the horizontal well as possible, and this may be achieved by drilling the horizontal well in the direction of minimum principal stress. Finally, the study of coupled primary-secondary fracture networks shows that during linear flow, the production from these coupled systems increases as the SRV increases. The production rates drop to about the same value with a reference primary fracture system during fracture-interference, and the pressure profiles show that this could be attributed to the very slow drainage of the unstimulated, low-permeability matrix surrounding the stimulated reservoir volume.

NOMENCLATURE

Variables:

A = Area of stimulated reservoir volume, ft^2
c_f = Formation compressibility, 1/psi
C_{fD} = Dimensionless fracture conductivity (dimensionless)
c_t = Total compressibility, 1/psi
d_f = Fracture spacing, ft
h = Reservoir thickness, ft
K = Matrix permeability, md
k_f = Fracture permeability, md
k_m = Matrix permeability, md
L_w = Horizontal well length, ft
p = Pressure, psi
p_i = Initial reservoir pressure, psi
p_r = Pressure at point r in reservoir, psi
p_{wf} = Wellbore flowing pressure, psi
q = Rate, bbl/day or mscf/day
q_D = Dimensionless rate
q_{Dd} = Dimensionless rate derivative (dimensionless)
q_{Ddi} = Dimensionless rate integral (dimensionless)
q_{Ddid} = Dimensionless rate integral derivative (dimensionless)
r = Radius, ft
r_D = Dimensionless radius (dimensionless)
r_w = Wellbore radius, ft
R = Ideal gas constant, 8.314 J/K-mol
S_w = Water phase saturation, fraction
S_G = Gas phase saturation, fraction
S_{airr} = Irreducible aqueous saturation of Corey *et al*.[8], fraction
S_{girr} = Gas phase saturation, fraction
S_{wi} = Initial water saturation, fraction
t = Time, days, hours or seconds
T = Temperature, K
t_D = Dimensionless time (dimensionless)
w = Fracture width, ft
x = Distance from production source, m
x_f = Fracture half-length, ft

Greek Symbols:

ϕ = Porosity, fraction

τ_G = Tortuosity (dimensionless)

ϕ_0 = Initial porosity, fraction

ρ = Density, kg/m^3

ρ_G = Gas phase density, kg/m^3

μ = Viscosity, cP

Subscripts:

G = Gas phase

CH4 = Methane component.

REFERENCES

Anderson, D.M., Nobakht, M., Moghadam, S. et al. 2010. Analysis of Production Data from Fractured Shale Gas Wells. Paper SPE 131787 presented at the SPE Unconventional Gas Conference, Pittsburgh, Pennsylvania, USA. doi: 10.2118/131787-MS

Bello, R.O. and Wattenbarger, R.A. 2008. Rate Transient Analysis in Naturally Fractured Shale Gas Reservoirs. Paper SPE 114591 presented at the CIPC/SPE Gas Technology Symposium 2008 Joint Conference, Calgary, Alberta, Canada. doi: 10.2118/114591-MS

Blasingame, T.A. and Poe Jr., B.D. 1993. Semianalytic Solutions for a Well with a Single Finite-Conductivity Vertical Fracture. Paper SPE 26424 presented at the SPE Annual Technical Conference and Exhibition, Houston, Texas, USA. doi: 10.2118/26424-MS

Cipolla, C.L., Lolon, E., Erdle, J. et al. 2009. Modeling Well Performance in Shale-Gas Reservoirs. Paper SPE 125532 presented at the SPE/EAGE Reservoir Characterization and Simulation Conference, Abu Dhabi, UAE. doi: 10.2118/125532-MS

Freeman, C.M. 2010. Study of Flow Regimes in Multiply-Fractured Horizontal Wells in Tight Gas and Shale Gas Reservoir Systems. M.S. Thesis, Texas A&M University, College Station, Texas, USA.

Freeman, C.M., Moridis, G.J., Ilk, D. et al. 2009. A Numerical Study of Performance for Tight Gas and Shale Gas Reservoir Systems. Paper SPE 124961 presented at the SPE Annual Technical Conference and Exhibition, New Orleans, Louisiana, USA. doi: 10.2118/124961-MS.

Gringarten, A.C. 1971. Unsteady-State Pressure Distributions Created by a Well with a Single Horizontal Fracture, Partial Penetration, or Restricted Entry. Ph.D. Dissertation, Stanford University, Stanford, California, USA.

Gringarten, A.C., Henry J. Ramey, J., and Raghavan, R. 1974. Unsteady-State Pressure Distributions Created by a Well with a Single Infinite-Conductivity Vertical Fracture. *SPE Journal* **14** (4). doi: 10.2118/4051-PA.

Houze, O., Tauzin, E., Artus, V. et al. 2010. The Analysis of Dynamic Data in Shale Gas Reservoirs - Part 1. Company report, Kappa Engineering, Houston, Texas, USA.

Jayakumar, R., Sahai, V., and Boulis, A. 2011. A Better Understanding of Finite Element Simulation for Shale Gas Reservoirs through a Series of Different Case Histories. Paper SPE 142464 presented at the SPE Middle East Unconventional Gas Conference and Exhibition, Muscat, Oman. doi: 10.2118/142464-MS.

Mattar, L. 2008. Production Analysis and Forecasting of Shale Gas Reservoirs: Case History-Based Approach. Paper SPE 119897 presented at the SPE Shale Gas Production Conference, Fort Worth, Texas, USA. doi: 10.2118/119897-MS.

Medeiros, F., Ozkan, E., and Kazemi, H. 2006. A Semianalytical, Pressure-Transient Model for Horizontal and Multilateral Wells in Composite, Layered, and Compartmentalized Reservoirs. Paper SPE 102834 presented at the SPE Annual Technical Conference and Exhibition, San Antonio, Texas, USA. doi: 10.2118/102834-MS.

Miller, M.A., Jenkins, C.D., and Rai, R.R. 2010. Applying Innovative Production Modeling Techniques to Quantify Fracture Characteristics, Reservoir Properties, and Well Performance in Shale Gas Reservoirs. Paper SPE 139097 presented at the SPE Eastern Regional Meeting, Morgantown, West Virginia, USA. doi: 10.2118/139097-MS.

Moridis, G.J., Blasingame, T.A., and Freeman, C.M. 2010. Analysis of Mechanisms of Flow in Fractured Tight-Gas and Shale-Gas Reservoirs. Paper SPE 139250 presented at the SPE Latin American and Caribbean Petroleum Engineering Conference, Lima, Peru. doi: 10.2118/139250-MS.

Palagi, C.L. and Aziz, K. 1994. Use of Voronoi Grid in Reservoir Simulation. *SPE Advanced Technology Series* **2** (2). doi: 10.2118/22889-PA.

Romain, M., Caumon, G., Levy, B. et al. 2011. Building Centroidal Voronoi Tessellations for Flow Simulation in Reservoirs Using Flow Information. Paper SPE 141018 presented at the SPE Reservoir Simulation Symposium, The Woodlands, Texas, USA. doi: 10.2118/141018-MS.

Rycroft, C.H. 2007. Multiscale Modeling in Granular Flow, Ph.D. Dissertation, Massachusetts Institute of Technology, Cambridge, Massachusetts,USA.

Shelley, R.F., Lolon, E., Dzubin, B. et al. 2010. Quantifying the Effects of Well Type and Hydraulic Fracture Selection on Recovery for Various Reservoir Permeabilities Using a Numerical Reservoir Simulator. Paper SPE 133985 presented at the SPE Annual Technical Conference and Exhibition, Florence, Italy. doi: 10.2118/133985-MS.

U.S. Energy Information Administration (EIA). Feb. 2007. 2007 Annual Energy Outlook with Projects to 2030. p. 93. ftp://ftp.eia.doe.gov/forecasting/0383(2007).pdf.

Warlick, D.N., 2006. Gas Shale and CBM Development in North America. Oil and Gas Journal. **3** (11). 1-8. http://www.ogfj.com/index/article-tools-template/_printArticle/articles/oil-gas-financial-journal/volume-3/issue-11/features/gas-shale-and-cbm-development-in-north-america.html.

VITA

Name:	Olufemi Morounfopefoluwa Olorode
E-mail Address:	femorode@yahoo.com
Education:	Texas A&M University, College Station, Texas, USA M.S., Petroleum Engineering December 2011
	University of Ibadan, Oyo, Nigeria B.S., Petroleum Engineering June 2008
Address:	Department of Petroleum Engineering c/o Dr Blasingame Texas A&M University College Station, TX 77843-3116
Affiliations:	Society of Petroleum Engineers